Title

Synthesis and Application of Multicomponent Metal Nanostructure in a Colloidal System

Author

HA, HYUNDONG

Publication Date

2020

Peer reviewed|Thesis/dissertation

Synthesis and Application of Multicomponent Metal Nanostructure in a Colloidal System

By

Hyun Dong Ha

A dissertation submitted in partial satisfaction of the
requirements for the degree of
Doctor of Philosophy
in
Chemistry
in the
Graduate Division
of the
University of California, Berkeley

Committee in charge:
Professor A. Paul Alivisatos, Chair
Professor Peidong Yang
Professor Seung-Wuk Lee

Fall 2020

Synthesis and Application of Multicomponent Metal Nanostructure in a Colloidal System

Hyun Dong Ha

Abstract

Synthesis and Application of Multicomponent Metal Nanostructure in a Colloidal System

by

Hyun Dong Ha

Doctor of Philosophy in Chemistry

University of California, Berkeley

Professor A. Paul Alivisatos, Chair

Natural and artificial photosynthesis both require a precisely organized structure with multiple components for an efficient charge transfer pathway. The development of nanotechnology enables us to scale these sophisticated structures from bulk to nanometer-size by providing tunable physical and electronic properties. In order to achieve sophisticated nanostructures, lithographic techniques are commonly used to arrange those components in arbitrary patterns. However, lithographed materials are not easy to be scaled up, and it is hard to study the electronic picture due to the lack of well-defined facets and crystalline structure.

There has been a surge of interest in exploring the effect of metal colloidal nanoparticle in photochemistry. The localized surface plasmon resonance property of the metal nanoparticle generates energetic charge carriers above the fermi energy of the metal. Interestingly, the energy of the charge carrier is greatly dependent on the morphology of the structure which can harvest photons over the entire solar spectrum. However, since the lifetime of carriers is extremely short compared to the semiconductor nanoparticles, other components are required to capture the energetic electrons from the metal nanoparticle. Thus, sophistically incorporating multiple components on the metal nanoparticle offers an effective way to use hot carriers of the metal nanoparticle. These complex structures based on the metal nanoparticle can further shed light on diverse applications such as plasmonics and photocatalysis.

This dissertation lays out a novel synthetic approach to fabricate a function-oriented colloidal polyelement nanostructure using a solution-phase redox chemistry. Furthermore, we demonstrate that such a sophisticated nanostructure can effectively improve the photocatalytic efficiency of hydrogen and oxygen evolution reaction without the use of any scavenger.

I truly believe that this thesis work can inspire the material research community for the development of a new library to manipulate the chemical and physical properties of matter.

To my parents and my sister

Acknowledgements

First, I really appreciate Professor A. Paul Alivisatos for his entire support and advice. Whenever I talked with him, he has always tried to deeply understand my science and ask core questions which I have barely thought about. It always motivates me to sit down and think about the problems instead of keep doing experiment.

I must also thank Professor Peidong Yang and Professor Seung-Wuk Lee as my qualifying exam and thesis committee members for all of their helpful discussions and guidance in my research.

I appreciate my first mentors, Dr. David Litt and Dr. Matthew R. Jones. Unfortunately, DNA assembly project has not been completed, but they gave me clear directions and support for me to settle down in this lab.

I also thank another mentor Dr. Chang Yan. We have argued sometimes, but he has tried to help me to do right science. It was great fortune to work with him as a collaborator, a mentor, and a lab mate.

I have had many opportunities to work with other labs. First, I really appreciate Dr. Heinz Frei and Dr. Georgios Katsoukis. When we had really difficult time to measure the photocatalytic activity, they let us to measure it in their setup with huge guidance and fruitful discussions. Without them, I doubt that this project can be completed.

Also, I really appreciate Professor Martin Moskovits and Professor Syed Mubeen. They gave us critical feedbacks and guidance of our work.

I would also like to thank every member in Alivisatos group. It has been really pleasured to work with them. They have always tried to help each other and been eager to collaborate.

I would like to appreciate Negest Williams. Especially during this pandemic situation, we have solved many nonscientific problems. She has been always trying to help me to move on.

I also like to thank my undergraduate researcher, Dayoung Lee, for all of her hard work and her willingness to listen to me.

Throughout entire 5 years, I couldn’t get through without my fantastic friends, Sangjae Bae, Hanwook Kim, Donggun Lee, Saehong Park, Sanghyo Lee, Sangwon Kim, Hyokyung Ryu, Heewon Moon, Philjun Kang, and Jeeyoung Kim. They have always made my life lively.

I would like to thank Samsung scholarship to support my funding and give me a chance to meet all the other Samsung scholarship students every year.

Lastly, I would like to thank my parents Young Boo Ha and Jung Hee Kim, and my sister Mi Song Ha.

Table of Contents

List of Figures

List of Tables

Chapter 1

Introduction

One grand challenge in the fields of chemistry and material science is to construct materials with precise control over the placement of each component by building materials with properties that are well suited for a desired application. Although various synthesis of multicomponent nanostructure has been developed, it is still highly challenging especially in colloidal phase.[1–4]

"Multi-component nanostructures" can be defined here as hybrid structures composed of two or more distinctly definable condensed nanoscale domains, which are different in shapes, sizes, or materials. Compared to the single nanoparticle system, multicomponent structures can exhibit emergent physical or chemical properties that arise from specific arrangements of matter.[5,6] A key example in nature is the photosynthesis system.[7] Integrating multi-components in specific arrangements in natural photosynthetic system provides a sophisticate charge transfer pathway with minimal energy loss.

There are two arising questions by assembling the nano-building blocks to make multi-component nanostructures.

Which building block can we use? This question is the same as what property is interesting when we connect them each other. Nanoparticles that are in nanometer size range exhibit distinct optical and electronic properties.[8] For example, metal nanoparticles have unique plasmonic properties when the size of the metal is smaller than the wavelength of visible light. The way these nanomaterials interact with electromagnetic radiation provides huge interest to the science community.

How can we connect these building blocks? Chemists have solved this problem with a key factor "directionality". Directionality can be used in a variety of forms to build complex architectures with these building blocks. One example is that the formation of covalent bonds or non-covalent interactions can direct the degree of control for the final arrangement of the product. The charge distribution on the nanostructure can also guide the place to connect with other building blocks.

This thesis covers a novel approach to solve these two questions. It is broken into four subsequent chapters. Chapter 2 provides general backgrounds on the theory of plasmonics and the motivation of multiple component materials. Chapter 3 introduces a novel synthetic route to make a library of diverse multi-component nanoparticles via photodeposition. Chapter 4 discusses the photocatalytic application using five vital element nanoparticles. Chapter 5 looks to the future direction of these materials.

Chapter 2

Properties of Metal Nanostructures with Their Hybrid Structures

2.1 Overview

To consider "which properties we are going to use by synthesizing colloidal multicomponent metal nanostructures", we need to deeply understand the property of a building block, "metal nanoparticle". In the 1800s, Michael Faraday investigated that solution of nano-sized gold particle was red in color but bulk gold was yellow. In 1857, he gave a public lecture with the topic on the relationship between the optical properties of gold metal and its dimensions.[9] The interaction of light with the metal nanoparticle has been hugely interested and studied, especially when the size of the metal is reduced to less than or equal to the wavelength of incident light.[10] In this chapter, we will explore the basics in the field of plasmonics and synergistic properties when the metal is combined with other components.

2.2 Plasmonics in Metals

Plasmonics explore how electromagnetic fields can be confined over dimensions on the order of or smaller than the wavelength. It is based on the interaction processes between electromagnetic radiation and conduction electrons at metallic interface or in small metallic nanostructures. The plasmon resonance of the free electrons in the metal nanostructures can be understood by a simple mass-and-spring model.[11] The polarizability of conduction electrons on the surface of metal causes an electric dipole which can creates restoring forces pulling the electrons toward the other positively charged, side of the particle, and continuing the oscillation at the specific frequency. (Fig. 2.1) Here, mass is the mass of all the electrons in the particle, which is invariant with the size, but the spring constant is varying with size of the nanoparticle. The larger the particle is, the smaller spring constant is with weaker electrostatic interaction. This means that the larger nanoparticle has less vibration frequency.

The plasmonic responses of metal nanostructures can be precisely simulated by numerical algorithms such as finite-difference time-domain (FDTD) methods, and direct dipole approximations (DDA).[12] However, for metal nanoparticles which size is much smaller than the incident wavelength, quasistatic theories such as Gans theory can be applied for measuring plasmonic properties with dipolar modes.[13] Here, we approximate that electromagnetic field is same throughout the entire particle.

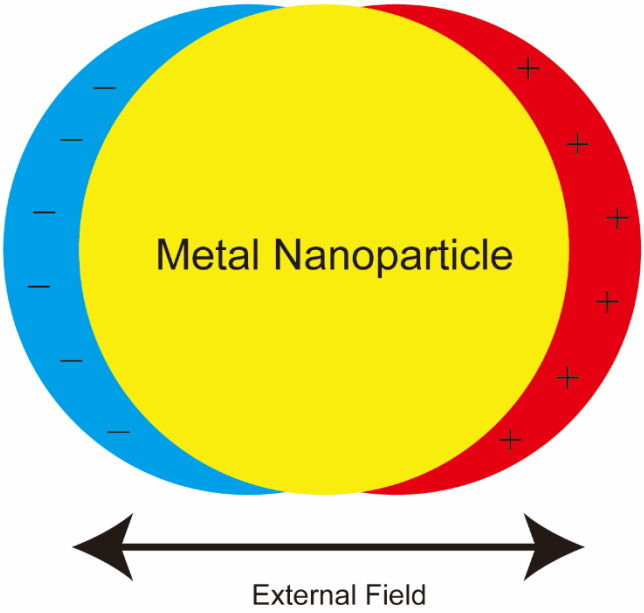

Figure 2.1. Schematic image of plasmon resonance of metal nanoparticle by the external field of light.

In this thesis, we normally focus on the gold nanorod (AuNR) system which has an anisotropic shape. The AuNR can be approximated as a prolate spheroid. By solving Laplace's equation in the ellipsoidal coordinate system, the scattering, absorption, and the extinction cross-section of an AuNR can be extracted.[13]

$$C_{sca,i} = \frac{k^4}{6\pi}|\alpha_i|^4 \quad (1)$$

$$C_{abs,i} = kIm(\alpha_i) \quad (2)$$

$$C_{abs,i} + C_{sca,i} = C_{ext,i} \quad (3)$$

$$\alpha_i = 4\,\pi abc\,\frac{\varepsilon_1 - \varepsilon_m}{3\varepsilon_m + 3L_i(\varepsilon_1 - \varepsilon_m)} \quad (4)$$

From these equations, k is the wavevector, α_i is the polarizability of the AuNR, ε_1 and ε_m are the dielectric functions of the surrounding medium and the gold. L value is the polarization factor which can be calculated by,

$$L_a = \frac{abc}{2}\int_0^\infty \frac{dq}{f(q)(a^2+q)} \quad (5)$$

$$L_b = \frac{abc}{2}\int_0^\infty \frac{dq}{f(q)(b^2+q)} \quad (6)$$

$$L_c = 1 - L_a - L_b \quad (7)$$

$$f(q) = \{(a^2+q)(b^2+q)(c^2+q)\}^{1/2} \quad (8)$$

In these equations, a, b, and c are the half lengths of the ellipsoid along the three major axes. Thus, from the equations above, scattering, absorption and extinction properties are varied with the size and shape of the particle.

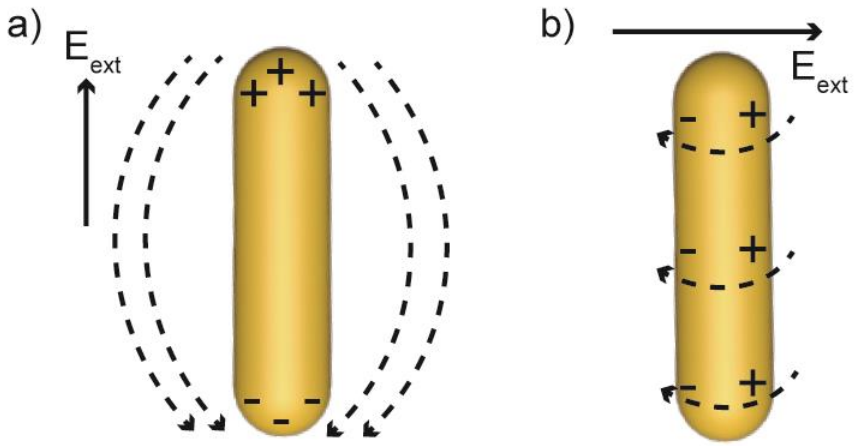

Figure 2.2. Schematic for the lowest-order longitudinal and transverse modes of a AuNR driven by an external field, E_{ext}.

Compared to the Au spherical nanoparticle, the AuNR has two different modes driven by the external field, E_{ext} due to the anisotropy of the geometry. When an external field drives the charge along the long axis of the NR, it supports the longitudinal modes, whereas it supports transverse modes when the charges are driven along the short axis of the NR. As shown in Fig. 2.2, the charge distributions of two different modes are significantly different. The longitudinal mode occurs at a much lower frequency than the transverse mode. Though these modes occur at discrete frequencies, they are strongly broadened due to the significant damping in the metal. Therefore, these modes are not truly discrete, but rather be thought of the resonances of the AuNR. By increasing the aspect ratio of AuNR, the extinction cross-sections of the transverse mode and the longitudinal mode of AuNR are increased and especially the wavelength of longitudinal mode is highly red-shifted. This is due to the higher polarizability of the nanorod at this mode. The polarizability usually defines how easily the nanoparticle can be polarized. The higher polarizability the nanoparticle has, the larger plasmonic peak shifts as their geometry is changed. Next chapter will cover the lifetime of the hot charge carriers generated by the metal nanoparticle.

2.3 Plasmon Decay Channel in Metal Nanoparticle

As we mentioned earlier, when the electrons of metal nanoparticle interact with electromagnetic wave, the electrons are coherently oscillating at a specific frequency. This is called localized surface plasmon resonance (LSPR). This resonance generated a sharp optical absorption or scattering along with strong electromagnetic fields. This LSPR decays both radiatively and nonradiatively. While the radiative decay of LSPR, which is the dephasing of the resonant oscillation, emits photons and transfers the radiated energy isotropically into the surrounding environment, the non-radiative decay of LSPR generates hot electron-hole pairs through electron-electron scattering. Due to the huge kinetic energies of them, the hot carriers generated by LSPR have been applied

to various applications such as sensing, catalysis, and imaging.

However, the decay of hot charge carriers from the metal nanoparticles is significantly faster than that of the electron-hole pairs from semiconducting nanoparticles. There are four decay dynamics of plasmon induced energetic charge carriers. 1) The plasmon decay occurs via Landau damping and generates hot electron-hole pairs. 2) Through the electron-electron scattering (< 100 fs), all the hot electrons relaxed from a non-Fermi to Fermi electron distribution. 3) The hot-electron gas is cooling and redistributed through electron-photon scattering (1-10 ps). 4) Lastly, all the heat will be dissipated from the metal nanoparticle to the dielectric environment via photon-phonon scattering (~ 100 ps).

Thus, in order to efficiently utilize the hot carriers of the metal nanoparticles, the hot carriers are required to either be consumed in the range of several hundreds of femtoseconds or be transferred to other material by capturing them to extend the lifetime of them. Next chapter will discuss how the interface of metal/metal oxide can prevent fast decay of charge carriers by forming the Schottky barrier between them.

2.4 Metal/Metal Oxide Nanoparticle

The most important factor to increase the transfer efficiency from metal to metal oxide is the ratio of electronic coupling between the hot electron and electron-accepting level.[14] The conduction band of metal oxides is normally well-aligned with Fermi level of the metal. Especially, TiO_2, which has a larger density of d-orbital states in conduction band than other metal oxides which mostly have s or sp orbitals, is the best candidate for the role of an electron filter. Also, metal and metal oxide generate the Schottky barrier in the interface which can prevent the recombination of the charge carriers.

One example we first fabricate is Au/TiO_2 janus nanoparticle using modified method by Seh et al.[15,16] We synthesize uniform Au nanospheres with the diameter of 80 nm as substrate materials. Seh et al. theoretically and experimentally demonstrated that the Janus geometry is the most energetically stable configuration when a small volume of the TiO_2 precursor is added.[16] Since the titanium diisoprpoxide bis(acetylacetonate) (TDAA) as a TiO_2 precursor is hydrophobic, it does not have a good wettability on the hydrophilic surface of the Au nanoparticle. This causes minimization of interfacial energy at the expense of elastic energy due to the bending of the nanorod by reducing the Au-TiO_2 interfacial area.

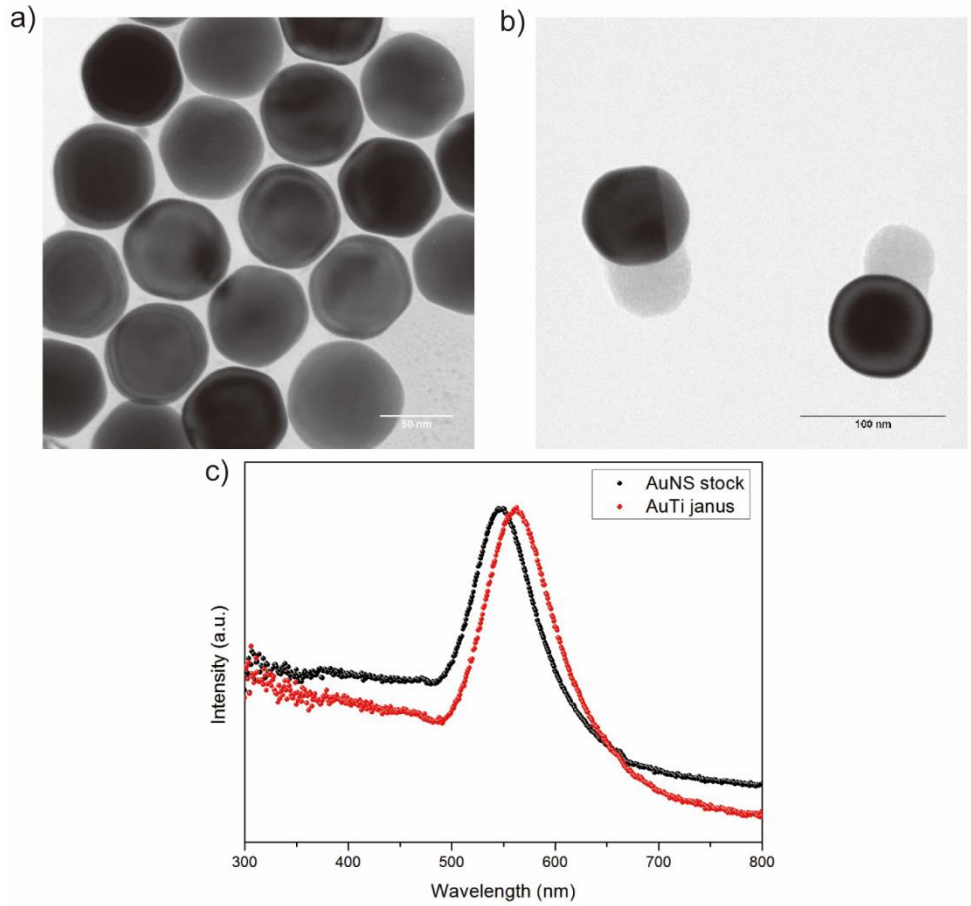

Figure 2.3. Janus typed Au/TiO_2 nanoparticle. HR-TEM images of a) Au nanospheres and b) Janus Au/TiO2 nanoparticles. c) UV-vis spectra of a) and b)

As shown in Figure 2.3b, the rest surface of Au nanoparticle is clean without any residue of TiO_2. Figure 2.3c also shows that the peak of LSPR is red-shifted due to the dielectric environment change of TiO_2. The refractive index of water and TiO_2 is 1.33 and 2.5 each. Higher refractive index medium causes the peak of LSPR to be red-shifted. The unique advantage of this geometry lies in the exposure of the gold core on one side, which provides direct contact to any chemical reactants for high catalytic rates. This geometric anisotropy causes hot electrons and holes to be separated; hot electron goes to TiO_2 and hole leaves behind Au. This type of building block can be extended to more complex structures using either reduction or oxidation reaction on the separated regions. Furthermore, there have been tremendous reports to study different shapes of Au nanoparticle in a colloidal system which can be used as a substrate material.[17,18] Next chapter will introduce a novel synthesis of polyelement nanoparticles in a colloidal system based on the AuNR via photo-redox chemistry.

Chapter 3

Photo-guided Polyelemental Plasmonic Nanostructure

3.1 Introduction

Compared to the single-component nanostructure, multi-component heterogeneous nanostructure can exhibit diverse properties such as chemical, electronic, and magnetic properties that do not arise in its counterpart. However, the integration of multiple components into a tiny nanoparticle has been extremely challenging due to an ensemble of individual phases of the components or the aggregation in an uncontrolled manner. There have been several routes to synthesize multiple polyelement nanoparticles, but it is not readily achieved in a large scale and in colloidal phase.[19–21] Herein, we introduce a novel synthetic route of complex polyelemental plasmonic nanostructure via photo-redox chemistry.

3.2 Principle of Photodeposition of Metal or Metal Oxide Nanoparticles in an Aqueous State

Photodeposition of metal or metal oxide on the substrate is based on light-induced electrochemistry where the substrate structure is illuminated with metal or metal oxide precursors in an aqueous system. A schematic diagram of both photoreduction and photooxidation is illustrated in Fig. 3.1.

A general equation for reduction of a metal M is[22]

$$M^{n+}(aq) + ne^{-} \rightarrow M(s) \qquad (1)$$

The photooxidation of metal oxide, MO is through

$$M^{n+}(aq) + nh^{+} + nH_2O \rightarrow MO_n(s) + 2nH^{+} \quad (2)$$

The key requirement is that the reduction/oxidation potential of metal or metal oxide must be favorable compared to the band position of the substrate. Thus, the conduction band of the substrate should be more negative than reduction potential of metal and the valance band of that should be more positive than the oxidation potential of the metal oxide. Also, the efficient charge separation and migration of light-induced electron-hole pairs are required. A huge advantage of the photodeposition is that this is a simple and clean method since it does not require the addition of reducing or oxidizing agents or any other conditions other than light exposure. There are various factors that affect photodeposition processes, such as metal precursors, sacrificial reagents, the influence of pH, and absence or presence of oxygen in the reactor.

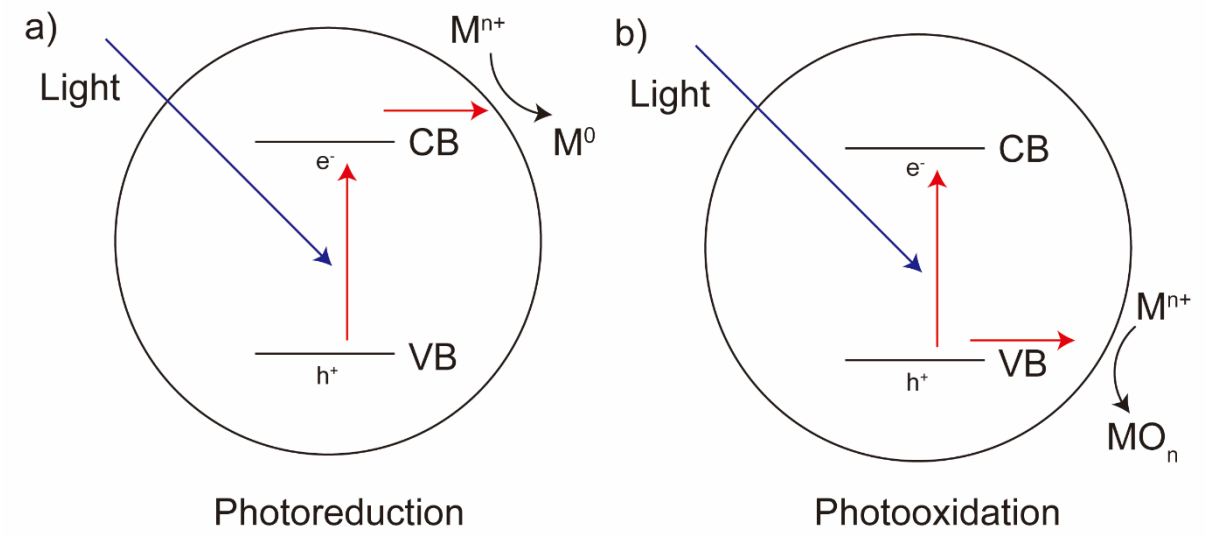

Figure 3.1. Schematic diagram of photodeposition methods; a) photoreduction and b) photooxidation process.

In our work, instead of using semiconducting nanoparticles, AuNRs interfaced with TiO_2 as an efficient electron acceptor are used as the substrate of photodeposition. As we discussed in Chapter 2, the plasmonic metal/semiconductor interface can selectively filter the hot electrons generated from surface plasmon due to the Schottky barriers in the interface. As depicted in Fig 3.2, when AuNRs are interfaced with TiO_2, the Schottky barrier between an n-type semiconductor and a metal is formed. Within this system, Φ_M is the working function of the metal which is defined as the energy needed to bring an electron from the metal Fermi energy to the vacuum; X_{SM} is the electron affinity parameter that is defined as the energy difference between the minimum conduction band (CB) and the vacuum energy (E_{vac}). Normally, the Fermi energy of metal is lower than that of the semiconductor. When they interface each other, the direction of electron flow will be preferably from the semiconductor to the metal. This flow will be continued until the Fermi energy of the semiconductor reaches to that of the metal. This deformation generates a potential barrier between them. This will cause depletion of electron at the semiconductor interface and form the positive space charge layer to maintain electrical neutrality at the interface causing the conduction band bending. This is called the Schottky barrier and which energy, Φ_{SB} is expressed by the following equation.[22]

$$\Phi_{SB} = \Phi_M - X_{SM} \qquad (3)$$

This Schottky barrier between metal and semiconductor can serve an effective hot electron trapping at the conduction band of semiconductor which prevent the charge recombination and prolong the lifespan of the electron. These trapped electrons can be used for photoreduction of metal nanoparticles, and the holes behind can be used for photooxidation of metal oxide nanoparticles.

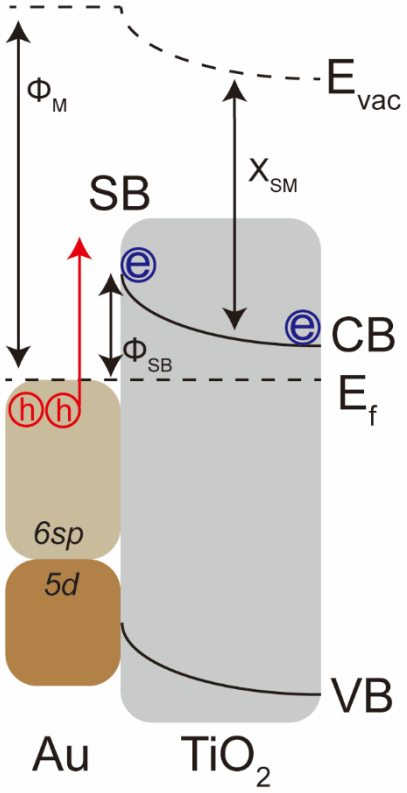

Figure 3.2. Schematic energy band diagram of Au/TiO_2 nanoparticle. Φ_M is the working function of Au, Φ_{SB} is the Schottky barrier, and X_{SM} is the electron affinity of TiO_2.

3.3 Results

3.3.1 Synthesis of Gold Nanorods

In order to fabricate Au/TiO_2 nanodumbell structure, the gold nanoparticle itself needs to be anisotropic. The AuNR is one of the best candidates for a starting material to deposit TiO_2 on the tip due to the different ligand distribution on the tip and the side. In the presence of cetyltrimethylammonium bromide (CTAB), the CTAB weakly binds {111} facets of the face-centered cubic crystal of the gold seed particle. Therefore, the distribution of CTAB on the surface can guide the growth of nanorod shape with {111} facets at the ends. The common synthesis of gold nanorod is followed. Small gold seed particles are synthesized by reducing gold chloride with sodium borohydride in a saturated CTAB solution. Then, the seed solution is diluted into the growth solution including gold chloride, CTAB, ascorbic acid, and silver nitrate. Small portion of silver nitrate placed near the surface helps higher homogeneity of nanorod shape than spheres, but the role of silver nitrate in the synthesis of AuNR is still argued.

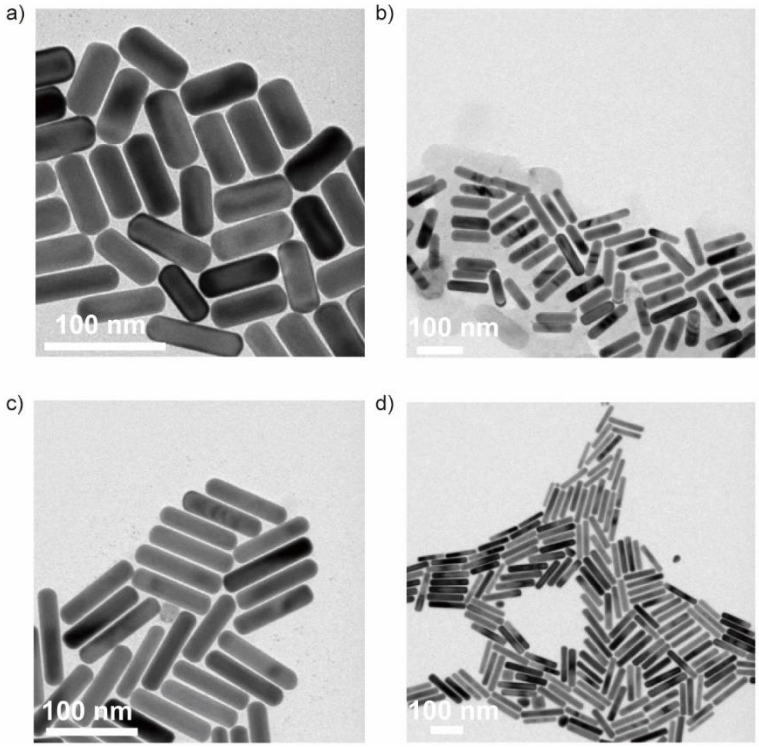

Figure 3.3. TEM images of synthesized AuNRs with different aspect ratio. a) 26 x 62 nm, b) 21 x 76 nm, c) 21 x 86 nm, and d) 20 x 111 nm. Each aspect ratio is 2.5, 3.5, 4, and 5.5.

Contrary to the other reported methods, Ye at al. added second surfactant, sodium oleate (NaOL), to the growth solution with CTAB to achieve the high quality of AuNRs.[23] Here, the key of this synthetic method is NaOL that is additional surfactant which can gently reduce molecules to turn Au(III) into Au(I) before adding ascorbic acid. This can prevent the generation of different nucleated particles during the growth of AuNR. Also, he tuned the pH of the growth solution to be acidic to get high quality of AuNRs. By changing pH, Ag, CTAB, and NaOL, different diameter, length, and aspect ratio of AuNRs can be fabricated in high quality. The TEM images of the synthesized AuNRs with different aspect ratio are shown in Fig. 3.3. The detail synthetic procedure is reported in Appendix 3.1.

3.3.2 Synthesis of AuNR/TiO_2 Dumbbell Structure

AuNR/TiO_2 nanodumbbell structure is fabricated by reported hydrolysis method.[24] As we mentioned earlier, this janus-type particles are obtained by different ligand distribution on the tip and side of AuNR. CTAB ligands which are bilayers of surface-capping agents, are more densly packed on the side than at the tips. Therefore, TiO_2 is anisotropically overgrown on the tips due to the different degree of hydrolysis of $TiCl_3$. Hydrolysis of TiO_2 is followed by the equation.

$$Ti(OH)_3 \rightarrow TiO_2 + H_2O + 0.5H_2 \qquad (4)$$

As shown in Fig. 3.4, by controlling the rate of hydrolysis with $NaHCO_3$ tuning pH, Ti^{3+} is catalytically oxidized on both tips of AuNR to form the nanodumbbell structure. The TiO_2 caps are uniformly coated on the edge of AuNR and the lateral side of AuNR is exposed. The enlarged TEM image of Au/TiO_2 in Fig. 3.5 confirms the homogenity of this dumbbell structure. The deposited TiO_2 is porous and amorphous structure which have high surface area to absorb chemical moieties.

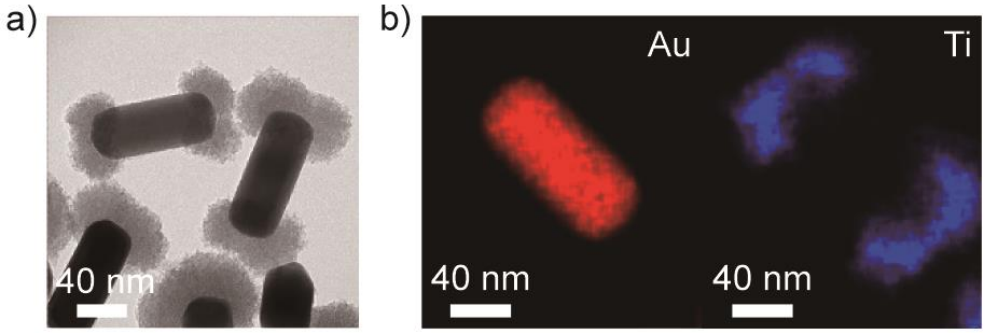

Figure 3.4. (a) TEM image and (b) elemental maps of Au/TiO_2 nanostructure.

The size of the TiO_2 caps can be controlled with different amount of $NaHCO_3$ and different carbon chain ligands. Figure 3.6 shows that higher pH in the solution causes higher ratio of the hydrolysis of $TiCl_3$ generating the larger covered area of TiO_2 on the AuNR. If the area of AuNR surface is covered less than 20 %, the colloidal stability of the solution significantly decrease which can cause irreversible aggregation. Therefore, the area of bare surface on the lateral side and the colloidal stability should be balanced. Also, as shown in Figure 3.7, we tuned the different carbon chain ligand on the surface of AuNR to tune the ratio of hydrolysis. As expected, longer carbon chain ligands cause less covered area of TiO_2 cap on the surface of AuNR, since the longer carbon chains hinder the precursor of TiO_2 to approach the surface of the AuNR.

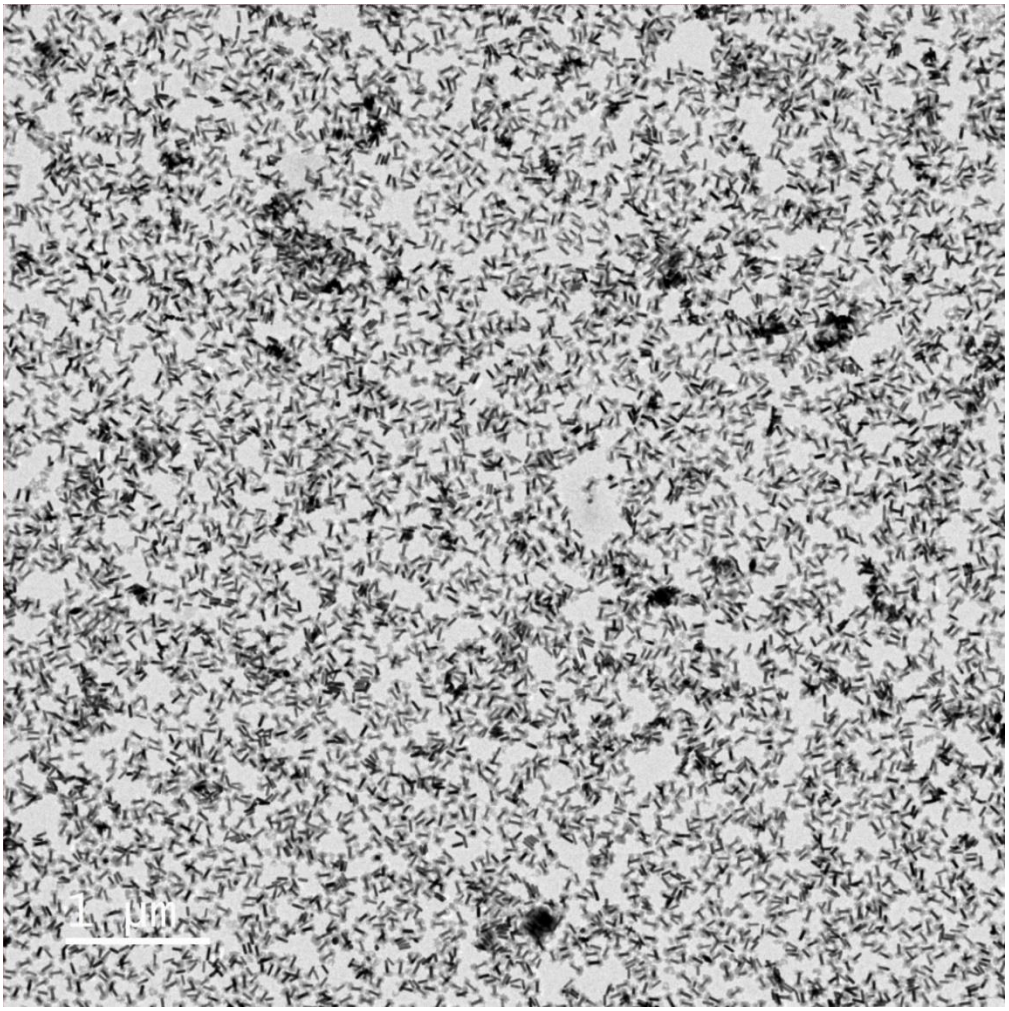

Figure 3.5. Large-scaled area of Au/TiO_2 nanodumbbell structure.

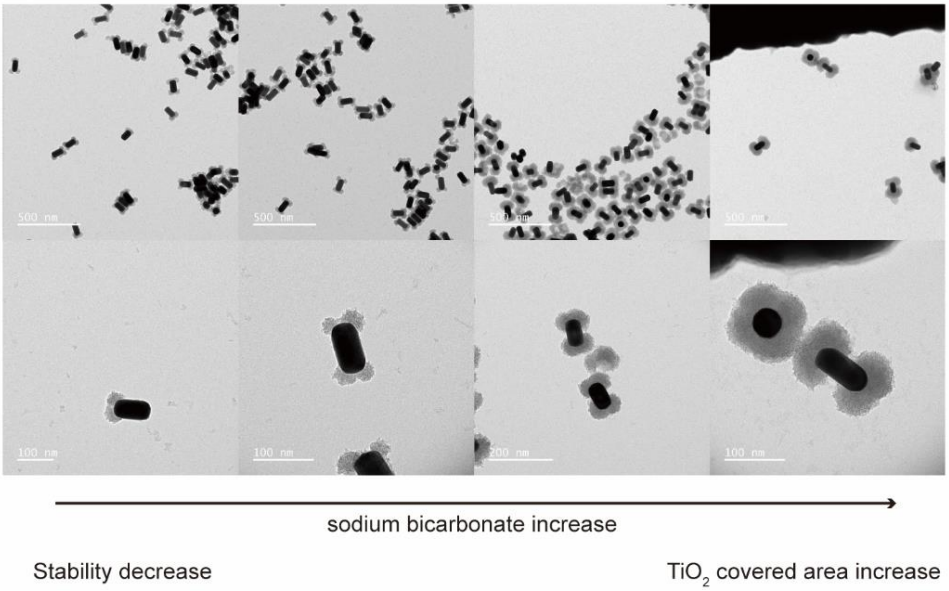

Figure 3.6. TEM images of Au/TiO_2 nanostructure with different amount of sodium bicarbonate.

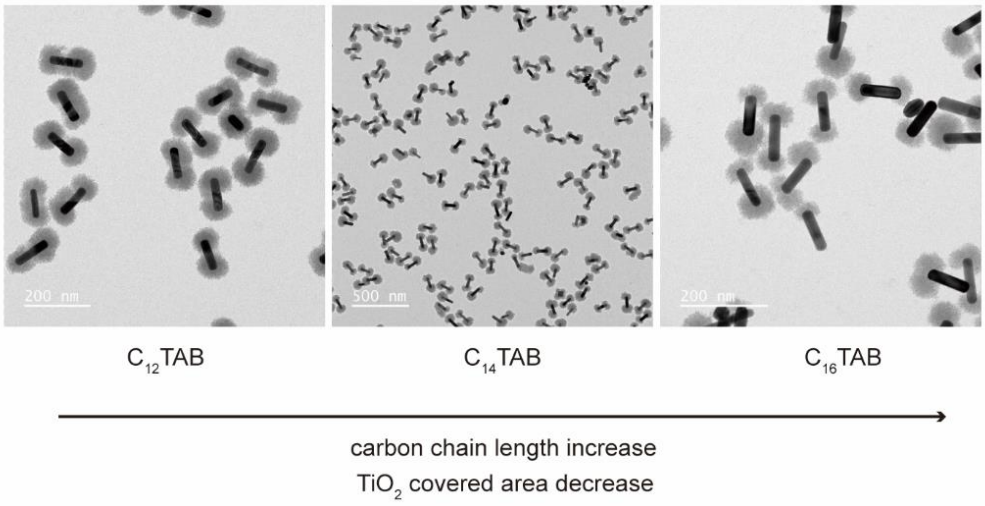

Figure 3.7. TEM images of Au/TiO_2 nanostructure with different carbon chain legands.

As we learned from chapter 3.3.1, different aspect ratio of AuNR has different LSPR peak of the absorption spectrum. Interestingly, Halas et al. reported that the electron transfer efficiency, $\emptyset_{inj}$, from metal to semiconductor can be calculated by[25]

$$\emptyset_{inj} = C_F \frac{(h\nu - q\varphi_B)^2}{h\nu} \qquad (5)$$

where C_F is the Fowler emission coefficient, $h\nu$ is the photon energy, and $q\varphi_B$ is the Schottky barrier energy. According to this equation, there are three parameters which can increase the electron transfer efficiency; One is increasing the photon energy, another one is decreasing the work function of the metal, and the last one is increasing the electron affinity of metal oxide. Increasing photon energy of e-h pairs generated from AuNR can be solved by tuning the aspect ratio of AuNR. The smaller aspect ratio of AuNR is, the larger energy of the charge carrier is. Thus, we generate various aspect ratios of Au/TiO_2 nanostructure from 2.5 to 5.5 as shown in Fig. 3.8. The approximate charge transfer efficiencies of each aspect ratio are calculated and shown in table 3.1 assuming that all parameters are fixed except the aspect ratio. If the SPR energy of Au/TiO_2 nanostructure is less than 1.1 eV which is the energy of Schottky barrier, negligible amount of hot electron is transferred to the conduction band of TiO_2.

Aspect ratio	2.5	3.5	4	5.5
SPR energy (eV)	1.86	1.54	1.38	1.18
$\emptyset_{inj}$	~0.39	~0.19	~0.1	~0.02

Table 3.1. Calculation of the approximate charge transfer efficiencies of Au/TiO_2 nanostructures depending on the aspect ratio

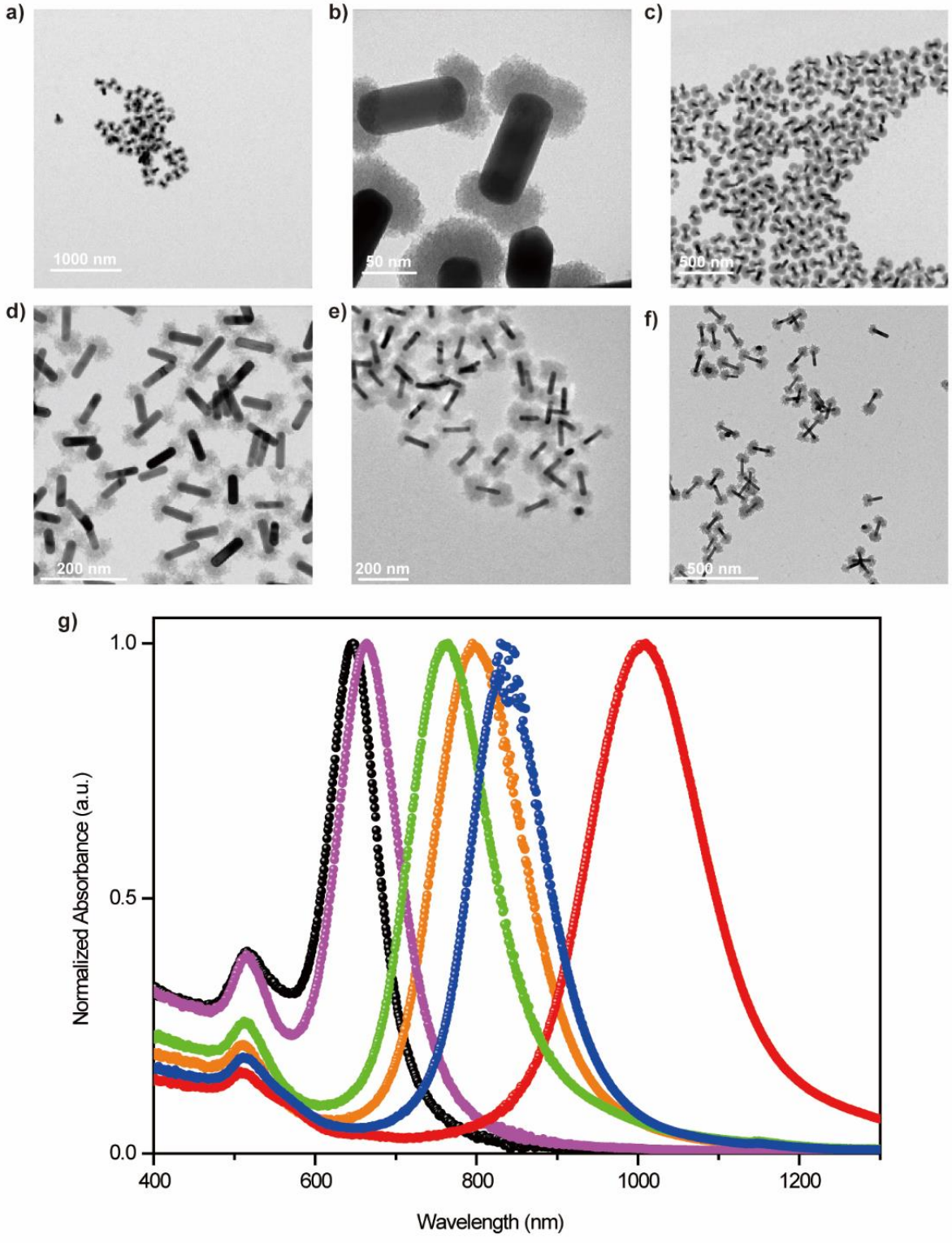

Figure 3.8. a-f) The TEM images of various dimensions of Au/TiO_2 dumbbell nanostructure (n=2). g) UV-vis spectra of each dumbbell nanostructure.

Metal	Work Function, Φ_M(eV)
Al	4.08
Zn	4.31
Fe	4.50
Cu	4.70
Ag	4.73
Au	5.10
Pt	6.35

Table 3.2. Values for work function of different metals

Among the metals, Ag, Au, Al, and Cu have been well-known plasmonic metals and their plasmonic modes are in the UV-visible region.[12] Referring to the table 3.2, the work function of the metal can be lowered if Ag, Al, or Cu is used.[26] Especially, Ag supports plasmon resonances with the lowest losses of all the metals in the visible-infrared spectral regions. However, Ag is easily oxidized and hard to be engineered to homogenous nanostructures. Therefore, this thesis use Au as the substrate material which have high chemical stability and chemical functionality.

The last parameter is to increase the electron affinity by either using the semiconductor with high density of state in its conduction band or having better band alignment with metal. Better contact between metal and semiconductor also increases the electron affinity. In this regard, TiO_2 has a huge density of d-band state which can accommodate a large density of hot electrons transferred from the gold nanoparticle.[27] Also, the overgrowth of TiO_2 on the gold can make a better contact between them. Therefore, the Au/TiO_2 nanodumbbell structure is one of the best platforms to study plasmonic charge carrier pathway and to be applied to the photocatalytic application.

3.3.3 Photodeposition of Au/TiO_2/Metal (n=3)

In order to deposit the metal nanoparticle on the caps of TiO_2 via photoreduction, the requirement is that the potential of the conduction band of TiO_2 is more negative than the reduction potential of the metal precursors. The examples of various reduction/oxidation potentials of metal precursors with the conduction band of TiO_2 are depicted in Fig 3.9.[22] Most of metals can be potential candidates for the photodeposition on the TiO_2.

There are two routes of depositing metals only on the TiO_2 with different light sources; we can either use the transferred hot electrons from AuNR to TiO_2 or use the directly excited electrons from the valence band of TiO_2. In this chapter, we introduce the latter route to only deposit the metal nanoparticle on the TiO_2 with UV light source to directly excite the e-h pairs of TiO_2. We first exchanged thiol modified polyethylene glycol (mPEG-SH) with CTAB on the lateral side of AuNR. This prevents undesired photodeposition of metal nanoparticle on the clean side of AuNR. We excited TiO_2 using 365 nm UV lamp with methanol as a hole scavenger with different metal precursors of Pd, Pt, Ag, and Cu with varied concentration. Only for 15 min duration of irradiation, the metal nanoparticles are significantly grown only on the TiO_2.

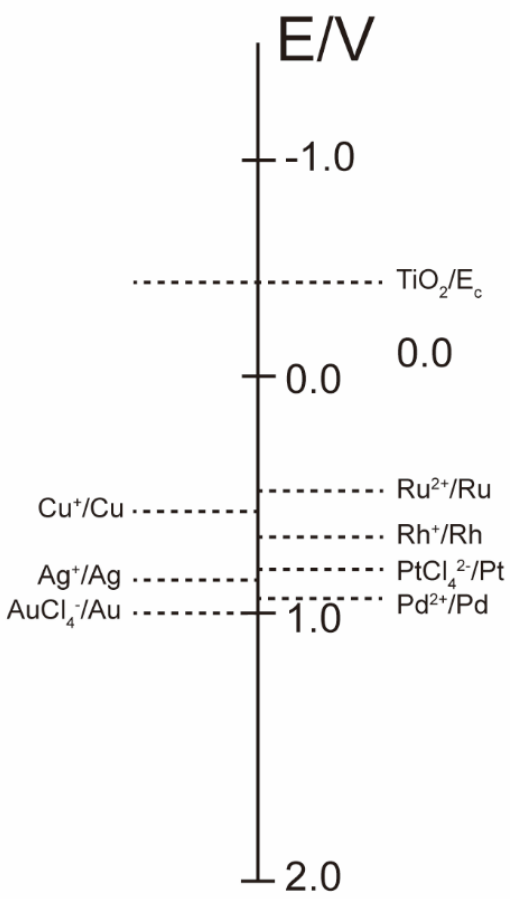

Figure 3.9. Reduction/oxidation potential of different metal precursors and conduction band energy of TiO_2

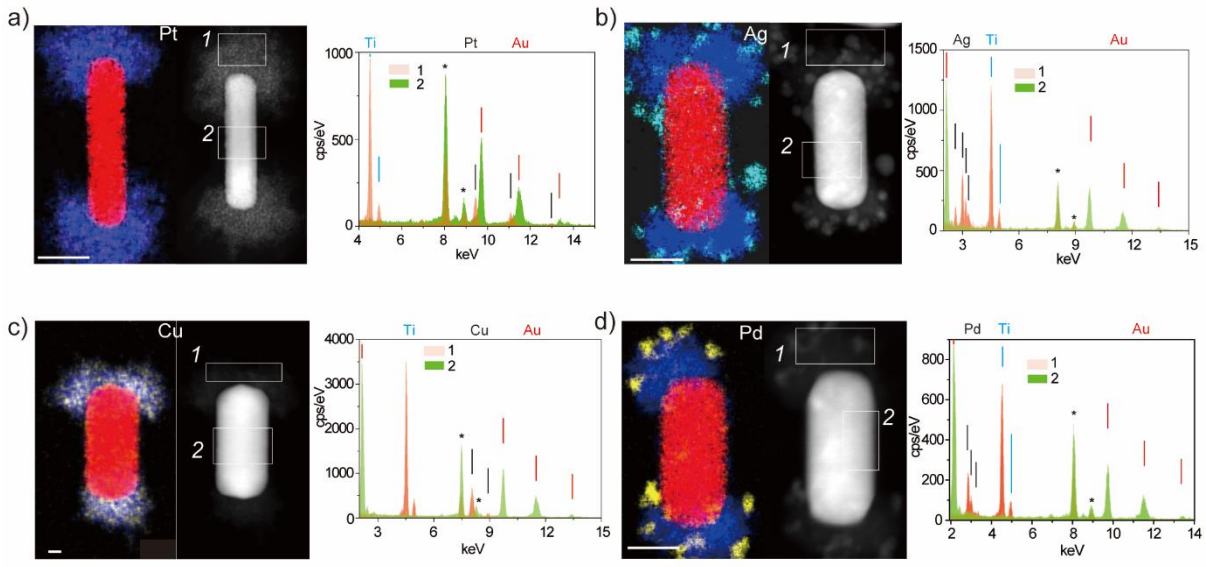

Figure 3.10. STEM-EDX maps of various polyelement nanoparticles with different metals, a) Pt, b) Ag, c) Cu, and d) Pd (left). EDX spectra of the cap region (red) and the central region 2 (green). Scale bar is 50 nm.

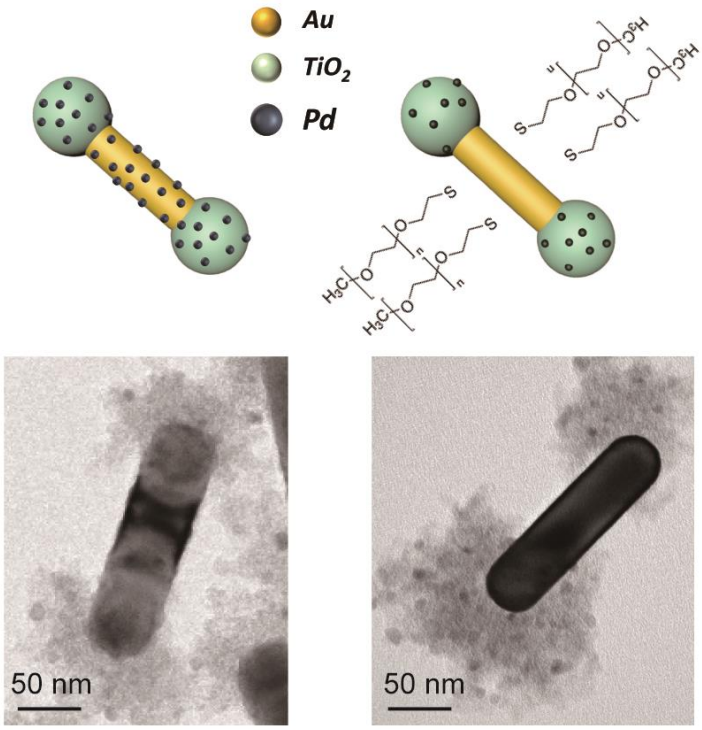

Figure 3.11. The schematic of Pd photodeposited on Au/TiO_2 nanodumbbell structure (left) with and (right) without mPEG-SH ligand exchange. (Bottom) The representative TEM images of each structure.

To characterize the elemental distribution of three-component nanostructures, energy dispersive x-ray (EDX) spectral mapping is performed using transmission electron microscope (STEM) under the high-angle annular dark-field imaging (HAADF) mode. EDX spectra are integrated and compared between the tip region and the central region. As shown in Fig. 3.10, Pd, Pt, Ag, and Cu signals are mostly observed in the tip region with Ti signal, whereas Au signal is mostly detected in the central region. These results clearly support the successful site-selective depositions of the metal.

To see the effectiveness of mPEG-SH, the photodeposition with the same setup without mPEG-SH is also evaluated. As shown in Fig. 3.11, if the lateral side of the AuNR is blocked by PEG-SH, the precursors of Pd are hard to approach the surface of the AuNR which can prevent the overgrowing on the lateral side of AuNR, whereas more Pd nanoparticles were grown on the side without mPEG-SH ligand.

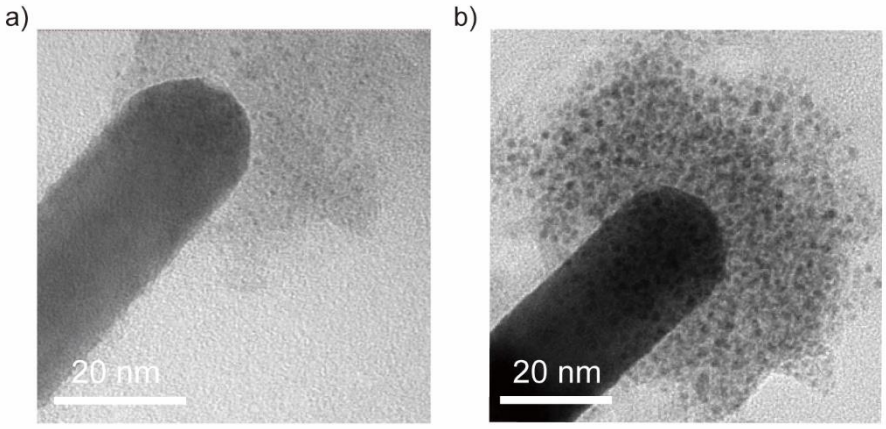

Figure 3.12. Investigation of effects on exposure time. a) 5 min and b) 15 min of UV exposure on Au/TiO_2 dumbbell structure with K_2PtCl_6 as the Pt precursor.

Different concentration of the metal precursor and the time duration of UV exposure can control the size and density of the metal nanoparticles. Fig. 3.12 shows that the density of Pt nanoparticle with 15 min of light exposure is much larger than that with 5 min of UV exposure. As shown in Fig. 3.13, the amount of the metal precursor produces similar effect with the duration of light. However, if there are excess amount of precursors, the metal nanoparticles start growing on the lateral side of AuNR.

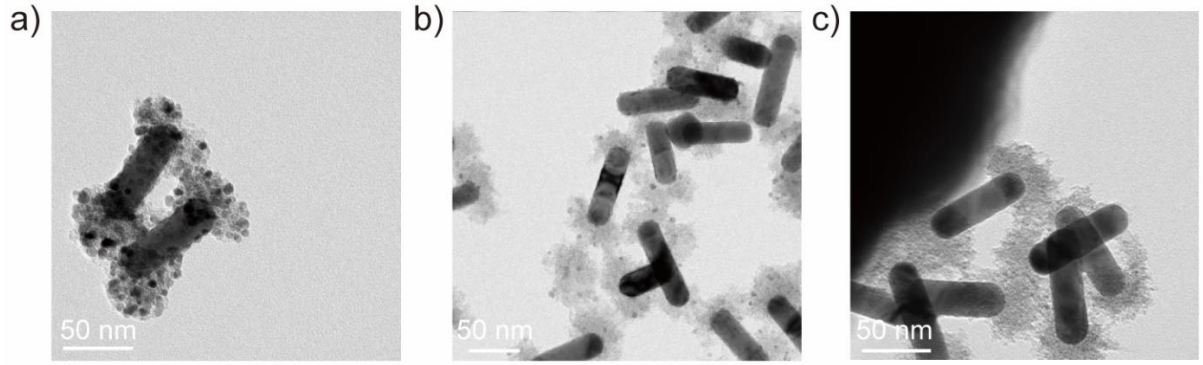

Figure 3.13. Investigation of effect on the precursor concentration. 15 min of UV exposure on Au/TiO_2 dumbbell structure with a) 100 μM, b) 25 μM, and c) 10 μM of H_2PdCl_4 as the Pd precursor.

3.3.4 Photodeposition of Metal Oxide/Au/TiO_2 (n=3)

As we mentioned earlier, to build more complicated structure with three components, we need to exploit separated e-h pairs in different regions. In this chapter, the hole left behind on the lateral side of AuNR is used to oxidize various metal oxide on it. Photodepositing metal oxide on the lateral side of AuNR does not need additional ligand passivation steps. Thus, with the metal oxide precursors and sodium persulfate as an electron scavenger, the metal oxide can be photodeposited only on the lateral side.

The CoO_x, which has been called cobalt oxygen evolving complex (Co-OEC)

including cobalt phosphate (Co-Pi) and cobalt borate (Co-Bi), has been extensively studied because it is efficient at near neutral pH through proton coupled electron transfer, which suggests similarities with OEC of natural photosystem.[28–30] The work on CoOx photodeposition has been extended to generate different metal oxide such as iron oxyhydroxide (FeOOH) on Au/TiO_2 dumbbell structure. FeOOH is one of sensible alternatives as Co-based cocatalyst for OER, since iron's abundance in the earth's crust behind only Si, Al, and O.[31,32] The Au/TiO_2 nanodumbbell structures were subsequently photooxidized by adding them with the metal oxide precursor, electron scavenger, and either using 0.1 M potassium borate buffer (pH 9.5) for CoOx, or using 0.1M K_2SO_4 for FeOOH. To avoid exciting TiO_2, we used broadband LED with 470-850 nm for exciting both interband and intraband transition of Au. Interestingly, with a very short amount of time (around 5 min) irradiation, the metal oxide was precisely guided to be oxidized only on the side of AuNR, meaning that the hot hole of AuNR was transferred and oxidized metal oxide precursor in the presence of electron scavenger and potassium borate buffer. As shown in Fig 3.14, Co, and Fe signals are mostly observed in the central region with Au signal, whereas Ti signal is mostly detected in the tip region. These results clearly support the successful site-selective depositions of metal oxide.

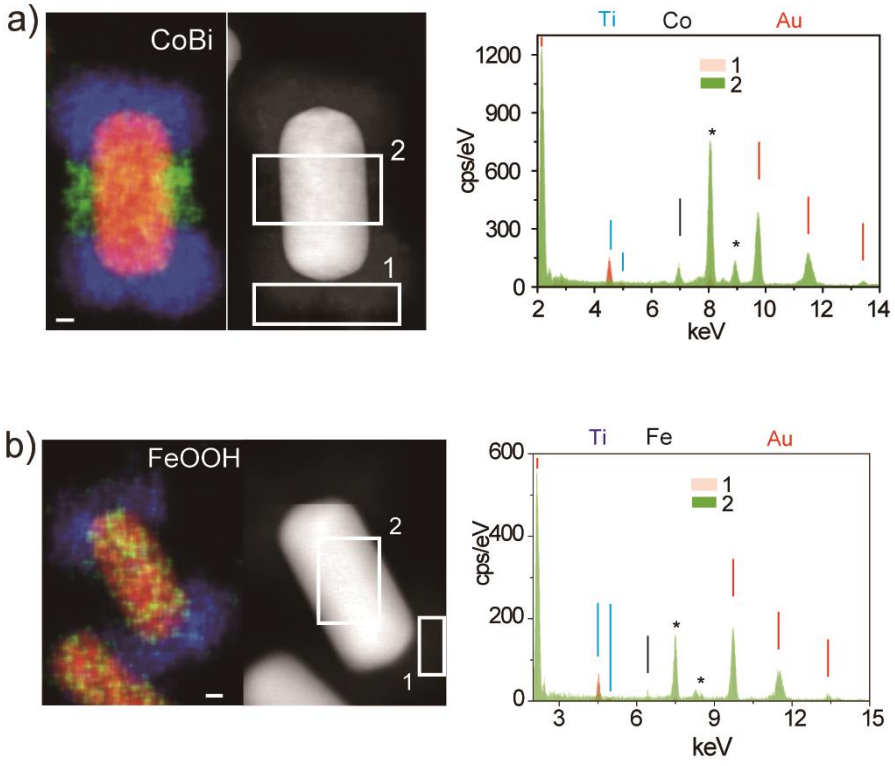

Figure 3.14. STEM-EDX maps of various polyelement nanoparticles with different metal oxides, a) CoO_x, and b) FeOOH (left). EDX spectra of the cap region (red) and the central region 2 (green).

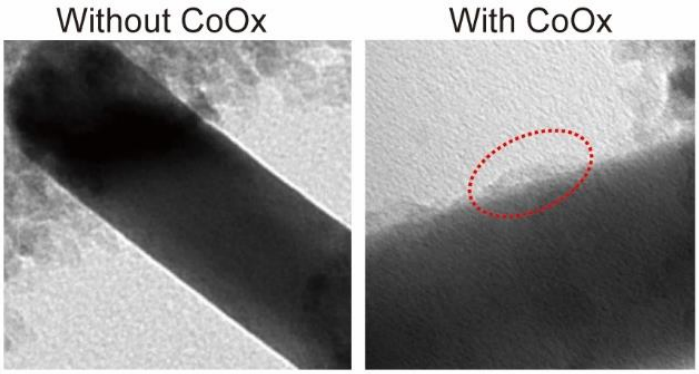

Figure 3.15. HR-TEM image of Au/TiO_2 without CoO_x (left) and with CoO_x (right) to show the growth of CoOx on the bare side of the Au NR.

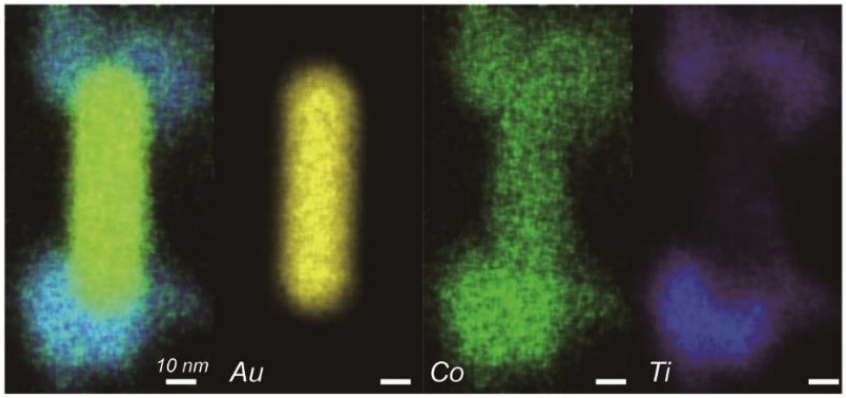

Figure 3.16. STEM-EDX maps of $Au/TiO_2/CoO_x$ deposited using 365 nm UV irradiation. Au-Lα, Co-Kα, and Ti-Kα lines shown as yellow, green, and blue. All the scale bars are 10 nm.

As shown in Fig. 3.15a and Fig. 3.15b, HR-TEM images of the structure with and without CoO_x, clearly show that the thin amorphous cobalt oxide film is deposited on the bare lateral side of the AuNR.

To confirm the light dependency of site-selective deposition, the 365 nm UV light is irradiated with the cobalt oxide precursors. As shown in Fig. 3.16, the CoOx is photodeposited on both the lateral side of AuNR and TiO_2. Since both charge carriers of AuNR and TiO_2 are excited by 365 nm UV irradiation, there is no site-selectivity of photodeposition. These results clearly provide further direction to synthesize more complicated structures with clear site-selectivity. Next chapter will cover the fabrication of nanoparticles including four components.

3.3.5 Photodeposition of Metal Oxide/Au/TiO_2/Metal (n=4)

We further extend the library by synthesizing quaternary comibinations of Au, TiO_2, metal, and metal oxide. There are two routes that we can further synthesize more complex nanoparticles. One is that photodeposition of metal is followed by that of metal oxide, and the other one is vice versa. The first route enables us to synthesize the quaternary nanoparticle without any further surface modification steps. The fourth component which is the metal can be simply photoreduced with metal precursors and hole scavengers irradiated by broadband LED with 470-850 nm. When excited by the broadband LED, transferred hot electrons on TiO_2 from the AuNR are reduced by metal precursors and holes left behind are oxidized by methanol. Fig. 3.17 clearly shows Co signal is mostly observed in the central region with Au signal, whereas Ti and Pd signals are mostly detected in the tip region. Elemental mapping is also performed at lower magnifications to confirm the homogeneity of these architectures (Fig. 3.18).

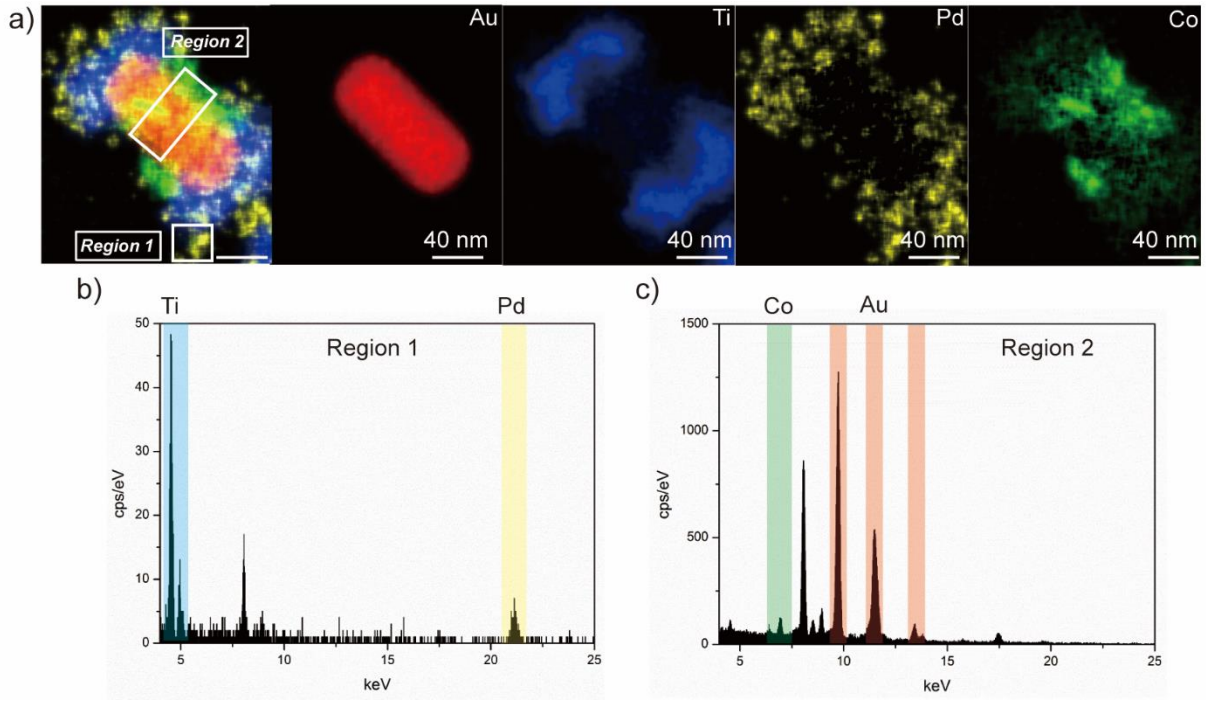

Figure 3.17. Quaternary nanoparticle. a) STEM-EDX maps of Au-Lα, Ti-Kα, Pd-Lα, and Co-Kα. EDX spectra of the cap region 1 (b) and the central region 2 (c). Undesignated peaks are Mo and Cu signals from background.

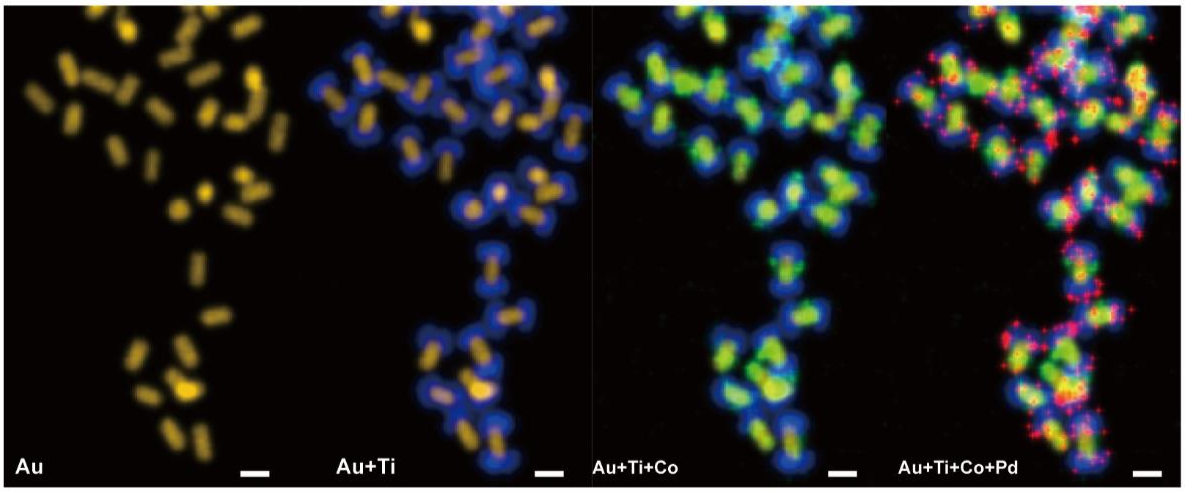

Figure 3.18. Lower magnification STEM-EDX maps of each component. Au-Lα (yellow), Ti-Kα (blue), Pd-Lα (red), and Co-Kα (green) lines. All the scale bars are 50 nm.

3.4 Conclusion

As shown in Fig. 3.19, two guidelines based on the structure anisotropy and redox chemistry can provide unimaginable complexity of the nanoparticle especially in a colloidal system. Further studies to discover the generality of each component are needed. Also, studying the interface between the components can enable us to better understand the charge transfer pathway.

There have been several reports to introduce syntheses of polyelemental nanoparticles. However, practical applications of these structures have been rarely reported. Next chapter will introduce a function-oriented nanoparticle for full water splitting with five components to essentially contribute the photocatalytic acitivity of water splitting. This will further shed light on the potential applications of these complicated structures.

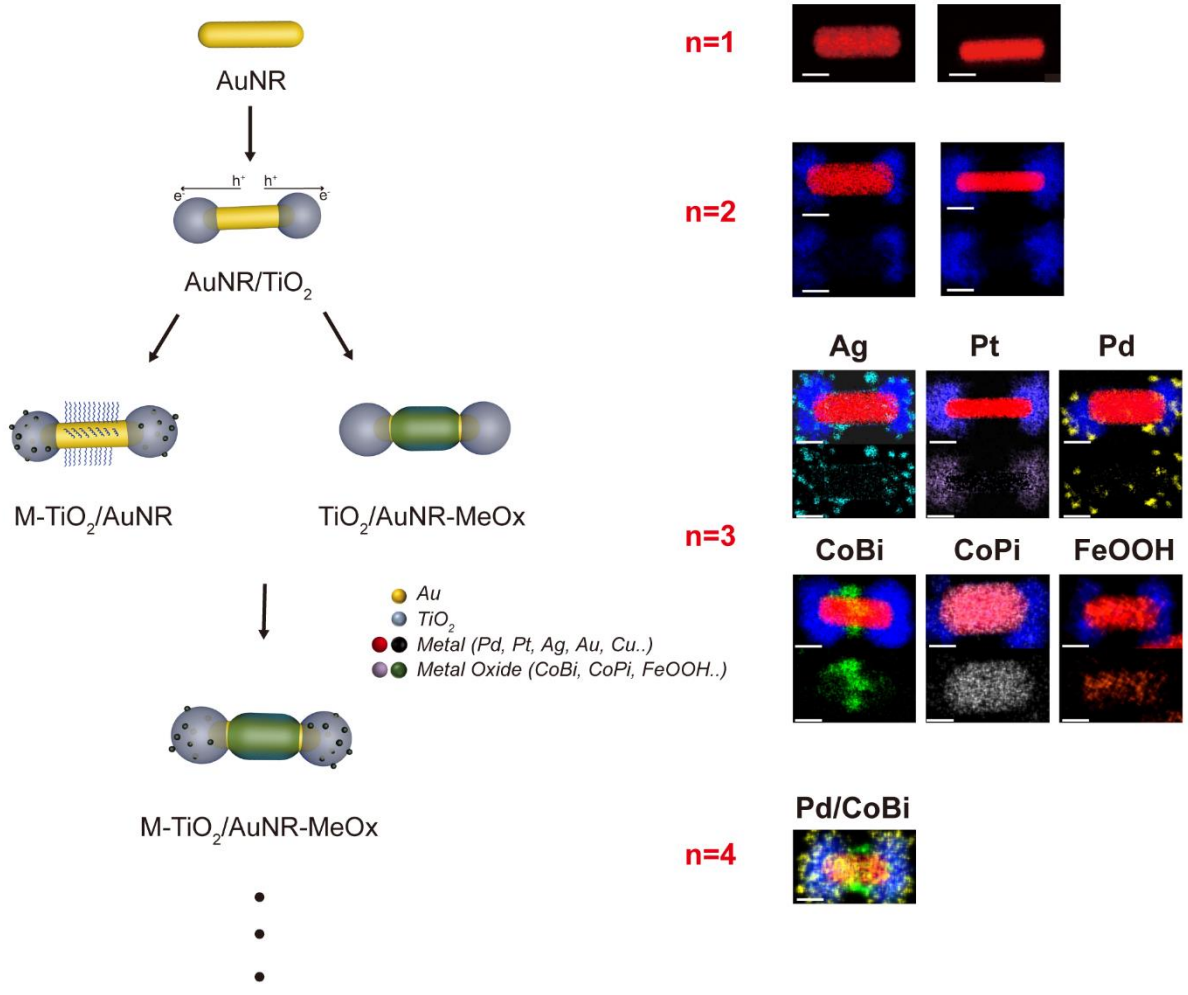

Figure 3.19. (Left) Schematic illustration depicting a four-element library of polyelement nanoparticles via photodeposition with adequate scavenger. (Right) Representative EDS mapping images of nanoparticles.

Chapter 4

Unassisted Photocatalytic Water Splitting by Precise Colloidal Plasmonic Nanostructures

Natural photosynthesis relies on a sophisticated charge transfer pathway among multiple components with precise spatial, energetic, and temporal organizations in the aqueous environment. It continues to inspire and challenge the design and fabrication of artificial multi-component colloidal nanostructures for solar-to-fuel conversion. Herein we introduce a plasmonic water splitter fully synthesized with colloidal methods with five integrated components including the hydrogen and oxygen evolution co-catalysts installed in orthogonal locations. Individual components are sequentially photodeposited on an AuNR via solution-phase redox chemistry. Under visible light solar irradiation, unassisted water splitting without scavengers is driven by the hot charge carriers derived from exciting both the d-sp interband transition and the localized surface plasmon resonance of Au. We verify that the hot electrons and hot holes generated from the two transitions flowed in a guided pathway similar to the Z-scheme mechanism.

4.1 Introduction

Utilizing solar energy to effectively generate renewable fuels is a significant challenge attracting wide scientific attention.[33,34] Both natural and artificial photosynthetic systems typically consist of multiple co-catalysts, charge acceptors, and light absorbers. An efficient design for solar-to-fuel conversion requires precise charge transfer pathways among different components. Such designs with high performance have been realized for lithographically fabricated structures used in photoelectrochemistry (PEC),[35–39] but they face some challenges for scaling to high volumes. Differently, natural photosynthesis machinery built from nanoscale structural units organized in a highly ordered fashion is available on a planetary scale but is still low in power efficiency.[40–42] Integration of all the artificial components to create a precise colloidal photosynthesizer remains extremely challenging with the current state of nanoscale synthesis, as it requires stringing together a particularly long series of orthogonal steps involving different inorganic materials.

There has been rapid progress in the synthesis and characterization of a large library of complex nanostructures containing multiple compositions including oxides, semiconductors, and metals.[2,43,44] For the purpose of promoting photocatalytic reactions, nanostructures with the anisotropic design to collect photo-generated electrons and holes at separated sites are highly desired. Efficient anisotropic photocatalysts with two or three components can be synthesized by leveraging the chemical reactivity of different inorganic components or nanocrystal facets. Some of the most advanced examples include metal-tipped CdS nanorods,[45] CdSe/CdS dot-in-rod structure with

metal tips,[46] and Pt-decorated Au/TiO_2 nanodumbells.[47,48] Another fabrication strategy is photochemical deposition which relies on the guided flow of charges in a semiconductor or metal nanocrystal to reduce or oxidize precursors at specific locations of a nanoparticle.[49–51]

Herein, we demonstrate that guided charge flow in the Au/TiO_2 nanodumbell structure can be harnessed to accurately photodeposit multiple inorganic components on either the TiO_2 tips or the lateral sites of the AuNR. The plasmonic excitation of Au NR can generate hot electrons to be collected on the TiO_2 tips, leaving holes on the Au NR. Therefore, the sites of photoreduction and photooxidation become well separated. With all the essential components, including Au, TiO_2, CoO_x, Pd, and Cr_2O_3, we construct a nanostructure with photocatalytic activity of oxygen evolution reaction (OER) from water without scavengers under visible light solar irradiation. Previously, colloidal plasmonic photocatalysts with fewer components have been shown to achieve hydrogen evolution reaction (HER) with hole scavengers.[52–54] To achieve the more challenging OER reaction without using scavengers, the synthetic problem of integrating more components into a colloidal plasmonic photocatalyst needs to be tackled. This work is inspired by the earlier top-down lithographic work of Moskovits et al., who fabricated a plasmonic PEC device for water splitting by integrating Au, TiO_2, CoOx and Pt.

Au plasmonic absorbers have many desirable properties for photocatalysis, such as large absorption cross-section, tunable spectrum over the visible wavelengths, and intrinsically high photostability.[55–57] The d-sp interband transition and the LSPR of Au can both provide charge carriers covering a wide range of energies.[58–61] In this work, we suggest that the photocatalytic OER without scavengers in water proceeds by combining the hot charge carriers derived from both the d-sp interband transition and the LSPR transition in a pathway resembling the Z-scheme in natural photosynthesis.

4.2 Structural Characterization

The architecture of the water splitter is shown in Fig. 4.1a. The Au NR harvests photons by LSPR and interband 5d-6sp transitions. Titanium dioxide caps on the two tips of the NR form two metal-semiconductor Schottky junctions to intercept the short-lived hot electrons generated from LSPR modes.[25,45] Upon photoexcitation, electrons are collected on the TiO_2 to perform reduction while the holes are orthogonally collected on the lateral sites to perform oxidation. A thin CoO_x layer is selectively deposited onto the lateral sites as the OER co-catalyst. Palladium nanoparticles are deposited onto the TiO_2 caps as the HER co-catalyst. Finally, a thin layer of chromium oxide is deposited onto the cap to cover the Pd nanoparticles. The design of a Cr_2O_3 layer blocks O_2 from reaching the Pd surface, and therefore prevents the back reaction. The CoO_x is installed by photooxidation of Co^{2+} precursor, while the Pd and Cr_2O_3 are installed by photoreduction of corresponding precursors. The clear separation of the reduction sites and the oxidation sites in the Au/TiO_2 dumbbell structure ensures the precise deposition of each component. This method does not require the selective surface passivation using

special ligands and is generalizable for depositing other metal or oxides.

Rarely a single optical absorption band could possess the suitable energy levels to drive both the HER and OER while covering well the solar wavelength range.[62] Natural and artificial photosynthesis systems often contain multiple absorbers in the HER and OER units working tandemly to power the overall reaction. Here the hot electron from the LSPR transition drives HER and the hot hole from the interband transition drives OER. The red arrow in Fig. 4.1b corresponds to the LSPR excitation generating a hot electron flowing across the Schottky barrier and a hole at the Fermi level of Au. The Fermi level of Au at +0.87 eV could not drive OER on CoO_x.[62] The interband transition associated with the blue arrow promotes an electron from the d band of Au to its Fermi level, forming a hot hole in the d band.[58] The electron at the Fermi level would not have enough energy to cross the Schottky barrier at the Au/TiO2 interface, whereas the hot hole deep in the d band could be extracted to CoOx to drive OER before cooling to the Fermi level.[63]

The absorption spectrum of water splitter in Fig. 4.1c is shown with the normalized spectrum of AM 1.5G solar simulator. The LSPR and interband transitions cover well the visible wavelength region from 400 to 800 nm. The LSPR band includes a minor transverse mode centered at 533 nm and a major longitudinal mode centered at 705 nm. The longitudinal LSPR mode associates with the electron oscillations along the long axis of the NR plays the major role for promoting the electron across the Schottky barrier.[64] The 5d-6sp interband transition of Au typically occurs for $\lambda < 520$ nm as indicated by the blue triangular area in Fig. 4.1c.[65] The Au NR was designed with a specific aspect ratio so that the two LSPR modes and the interband transitions separate well, allowing us to selectively excite each transition and investigate the charge transfer pathways. In figure 4.2, the peak shift of transverse LSPR and longitudinal LSPR of AuNR is shown along the consecative depositions. The longitudinal LSPR mode assoicates with the electron oscillations along the long axis of the rod, while the transverse LSPR mode is parallel to the short axis of the rod. When TiO_2 is deposited on the tip of AuNR, the longitudinal LSPR is highly red-shifted due to the higher dielectric constant of TiO_2 compared to water. On the other hand, when CoOx is deposited on the side of tip of AuNR, transverse LSPR is red-shifted due to the same reason. It clearly shows that the shift of longitudinal or transverse mode on the AuNR is indicative of a dielectric environment change depending on either transverse or longitudinal overgrowth.

Transmission electron microscope (TEM) images are displayed in Fig. 4.3a and 4.3b. The size of the Au NRs was 38 ± 4 nm in diameter and 92 ± 8 nm in length. Under careful examination, a 3-5 nm thin layer of deposits composed of mostly cobalt oxides can be observed coating on the sides of the Au rods. The spherical Pd nanoparticles on the TiO_2 caps have a diameter around 5-8 nm. Amorphous Cr_2O_3 could not be distinguished from the underlying TiO_2 caps due to similar contrast. To characterize the elemental distribution of the multi-component structure, energy dispersive x-ray (EDX) spectral mapping is performed using a scanning transmission electron microscope (STEM) under the high-angle annular dark-field imaging (HAADF) mode. EDX spectra are integrated and compared between the tip region and the central region (Fig. 4.3c-

4.3e). The Co and Au signals are mostly detected in the central region while the Ti, Cr, and Pd signals were mostly observed in the tip region. The EDX signals of each element are mapped onto the HAADF images of the two water splitters in Fig. 4.3f to demonstrate the site-selective installation of different components.

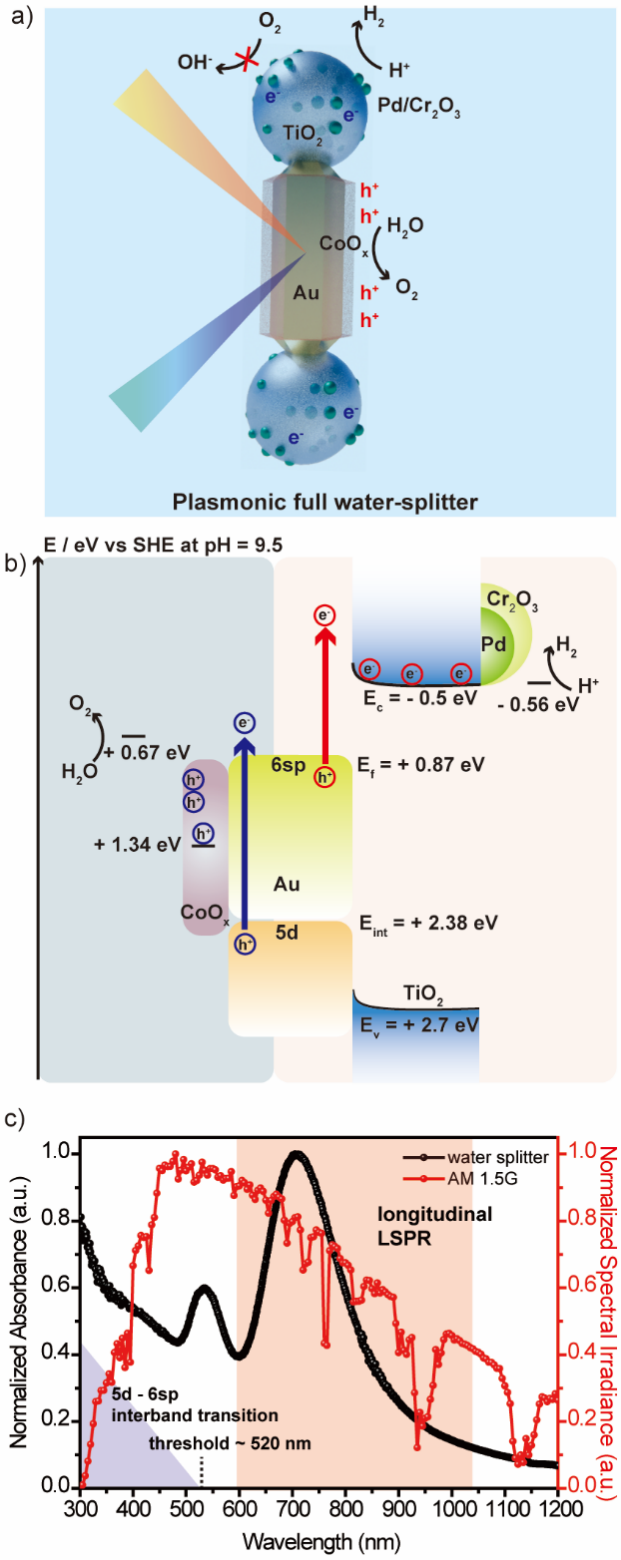

Figure 4.1. a) Schematic illustration of the design of the individual water-splitting unit. b) The proposed working principle of photocatalytic full-water splitting utilizing the interband and LSPR transitions. c) Normalized absorption spectrum of the water splitter (black) and spectrum of solar irradiation (AM 1.5G). Blue region shows 5d-6sp interband transition and red region shows the longitudinal LSPR transition.

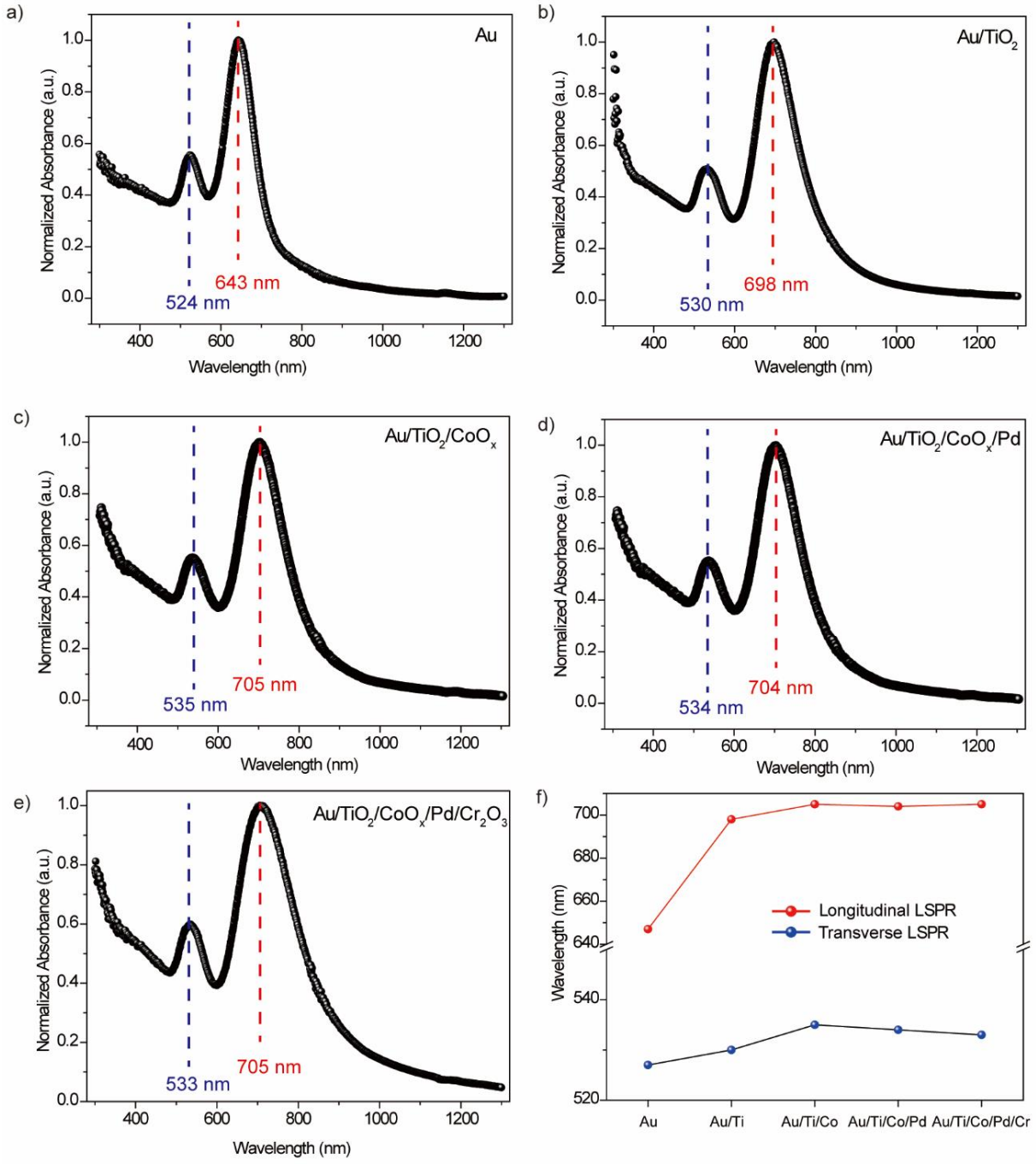

Figure 4.2. (a-e) The UV-vis absorption spectra of a) Au nanorod, b) Au/TiO_2, c) $Au/TiO_2/CoO_x$ d) $Au/TiO_2/CoO_x/Pd$, and e) $Au/TiO_2/CoO_x/Pd/Cr_2O_3$. The blue lines represent the transverse LSPR peak center and the red lines represent the longitudinal LSPR peak center associated with each structure. f) The peak center shift of longitudinal LSPR (red) and the peak shift of transverse LSPR (blue) during the successive depositions of each component.

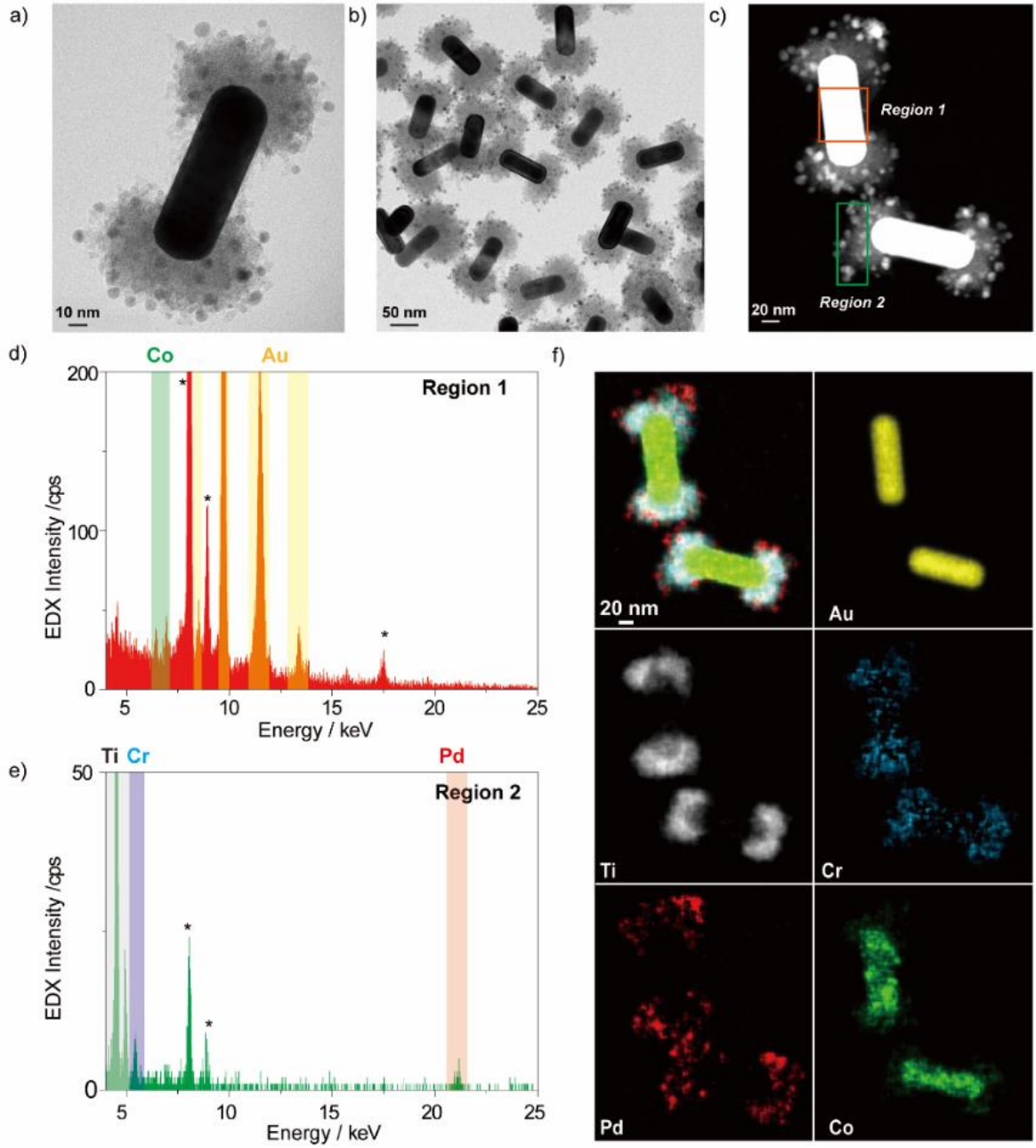

Figure 4.3. a-b) TEM images of the water splitter units. c-e) HAADF-STEM image (c) and EDX spectra of the cap region (d, orange) and the central region 2 (e, green). * denotes Mo and Cu signals from background. f) STEM-EDX maps of Au-Lα, Ti-Kα, Pd-Lα, Co-Kα, and Cr-Kα lines.

4.3 Photocatalytic Measurement

4.3.1. In Situ O_2 Evolution Measurement by Clark Electrode

The oxygen evolution of full water splitting and OER half reaction are analyzed by a calibrated Clark electrode system (Hansatech, Oxygraph system) with 700 mV applied.[66–68] The system composes of Pt cathode and Ag/AgCl anode with 0.1M KCl

aqueous solution as a supporting electrolyte. A thin O_2 permeable polytetrafluoroethylene (PTFE) membrane is used to separate the electrodes from the photocatalyst solution. Prior to the photocatalytic measurement, the silver electrode is thoroughly cleaned to remove brown/black silver oxide deposits and the Pt electrode is gently polished to maintain scratch-free surface.

Reaction of Ag/AgCl anode: $4Ag + Cl^- \rightarrow 4AgCl + 4e^-$ (1)

Reaction of Pt cathode: $O_2 + 4H^+ + 4e^- \rightarrow H_2O$ (2)

The test sample is prepared by diluting the photocatalyst stock solution in 0.1 M potassium borate buffer and is then sonicated for 10 min. 1.5 mL of the sample is loaded to the reactor with 1 cm path length and the optical density at 705 nm is set to 1. The concentration of the test sample is calculated by the reported extinction coefficient.[69] The calculated mass of the integrated photocatalyst in 1.5 mL is 28.4 µg. The temperature of the photocatalyst solution is controlled at 20 °C using a cool water jacket. For the OER half-reaction test, 50 mM $Na_2S_2O_8$ is included. Before irradiation, the test solution is bubbled with Ar gas to completely remove dissolved O_2. To confirm that O_2 is generated from the light-driven process, the irradiation of light starts after 20 min of flat zero O_2 concentration in a dark reactor under vigorous stirring.

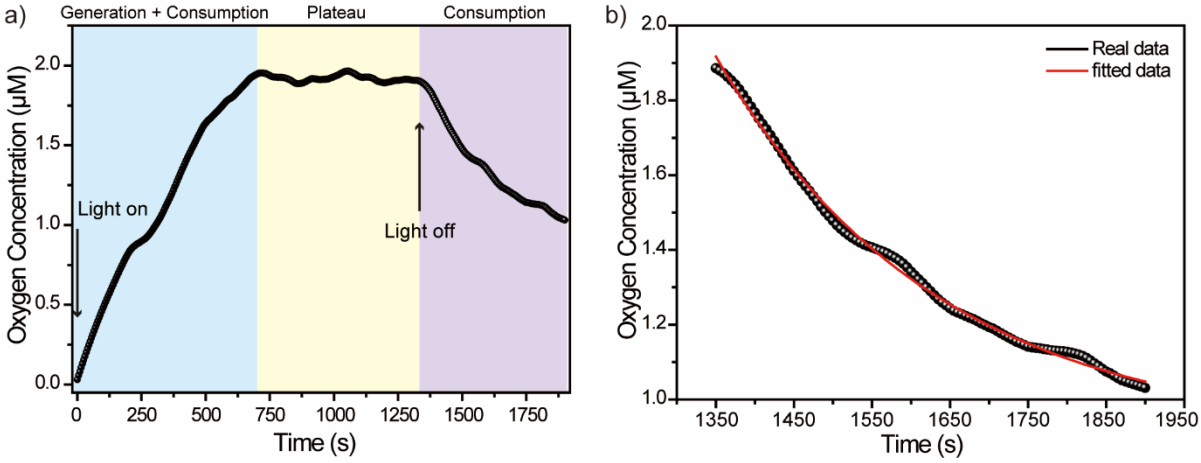

Figure 4.4. a) The entire cycle of O_2 generation from the integrated photocatalyst and O_2 consumption from the Clark electrode. Light on at 0 sec and light off at 1350 sec. O_2 generation and consumption region (blue), plateau region (yellow), and consumption region (purple). b) Fitting data of consumption rate at the Pt electrode after turning off the Xenon lamp (purple region in a).

A plot of the O_2 production rate is shown in Fig. 4.4a which corresponded to the data in Fig 4.5a (black line). We assume that the reactions are diffusion limited. The consumption rate of O_2 is proportional to the generated current (I_d) at the Clark electrode as expressed by equation 1.

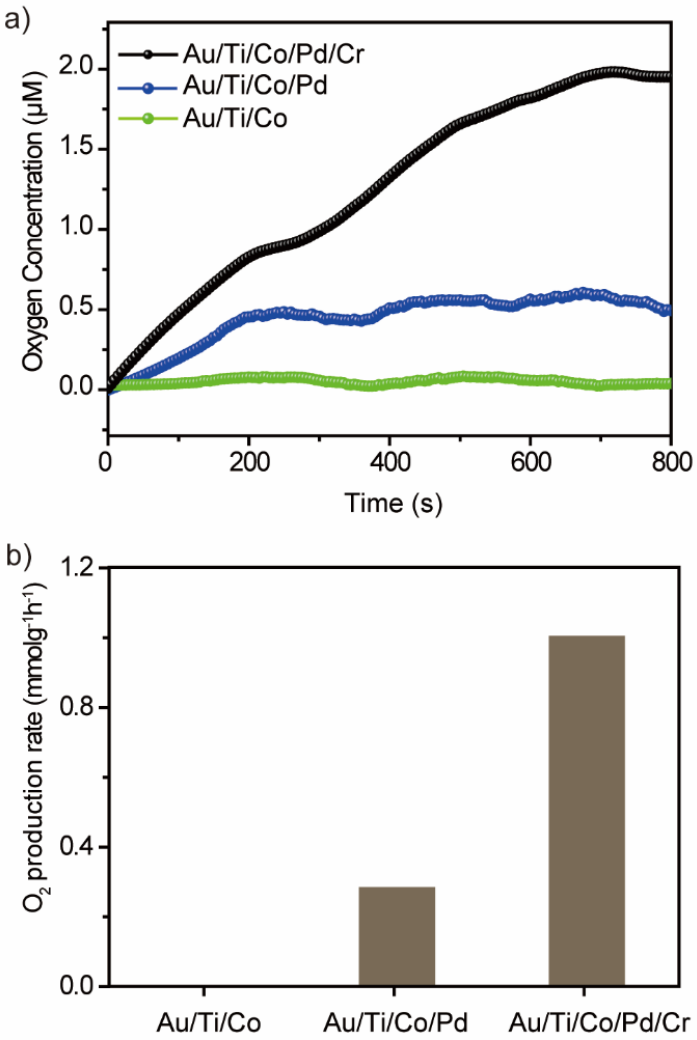

Figure 4.5. a) Water splitting performance monitored via in-situ oxygen concentration measurements. b) Comparison of the O_2 evolution rate by various nanostructures. c) The photocatalytic performance of the water splitter under different excitation conditions.

Upon light irradiation, the concentration of oxygen increases and reaches to plateau around 700 sec due to O_2 generation by our nanostructures and the simultaneous O_2 consumption by the Clark electrode. The kinetics are expressed in equation (2), where G is the oxygen generation rate. At 1350 sec, light is turned off and the concentration of oxygen decreases purely due to the consumption of remained O_2 in the test solution. By fitting the consumption kinetics to an exponential decay curve, the time constant of the exponential curve is determined as 284 ± 7 s ($R^2 = 0.99$, Fig. 4.4b). This consumption rate is related to the electrode settings and is found to be invariant for various samples. The consumption rate (k) of the Clark electrode is then -0.00352 s^{-1} ± 0.00008 s^{-1}. With the value of steady state concentration, the pure O_2 production rate (G) is calculated to 6.6 ± 0.15 nM·s^{-1}.

$$I_d = k[O_2] \qquad (3)$$

$$\frac{-\partial[O_2]}{\partial t} = k[O_2] - G \qquad (4)$$

The performance of the complete water splitter is compared with that of its precursors missing individual elements, and clearly demonstrates the necessity of incorporating all five components, each in their required position relative to the others (Fig. 4.5a and 4.5b). The O_2 evolution by $Au/TiO_2/CoO_x$ nanostructure is negligible due to the lack of HER sites. The deposition of cobalt oxide drastically improves the OER performance (Fig 4.6), but HER activity is still required to balance the full water splitting reaction. With Pd installed, the O_2 evolution rate of $Au/TiO_2/CoOx/Pd$ nanostructure reaches 0.28 $mmolg^{-1}h^{-1}$. Furthermore, the full water splitter with Cr_2O_3 shows a much higher O_2 evolution rate at 1 $mmolg^{-1}h^{-1}$. The fact that the Cr_2O_3 thin layer greatly improved the O_2 evolution rate suggests that back reaction of O2 on Pd surfaces was an efficiency-limiting factor. Domen et al previously reported similar effects of Cr_2O_3 layer deposited onto noble metals.[70–72] The Cr_2O_3 layer is permeable to water, hydrated protons, and H_2, but blocks O_2. The possibility of back reaction was not surprising since HER and OER sites in our nanostructured water splitter is only separated by tens of nm. The pure oxygen production rate is about 10^{-11} $mol \cdot s^{-1}$, and the upper boundary for the rate of photo absorption is 3.26×10^{-7} einstein s^{-1}. The lower boundary of the apparent quantum yield, defines as 2 × (4 × rate of O_2 generation) / (rate of photon absorption), is calculated as 0.024% for the full water splitter.

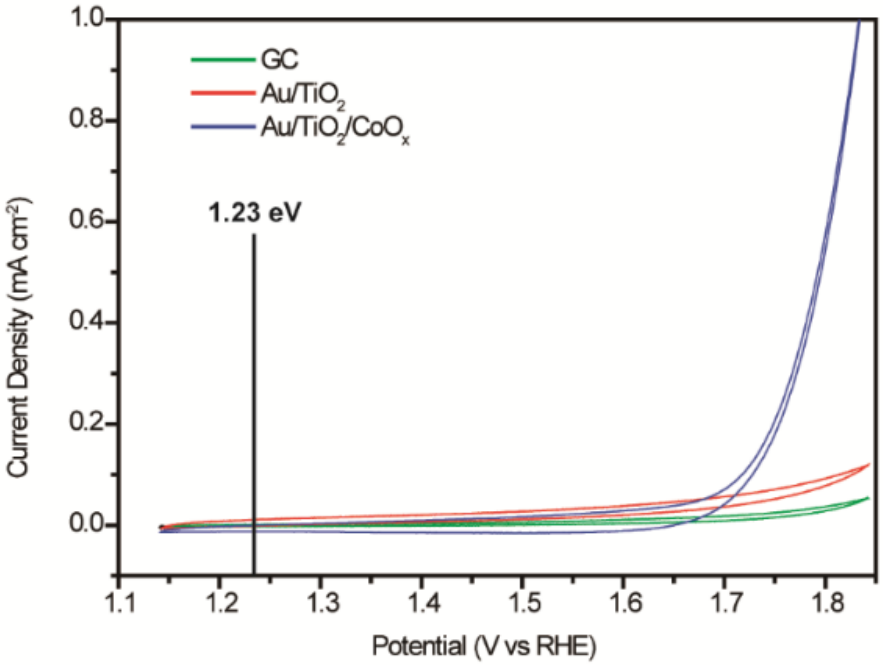

Figure 4.6. Electrochemical behavior of $Au/TiO_2/CoO_x$ and Au/TiO_2 nanodumbbell structure, and a bare glassy carbon electrode. The cyclic voltammetry data was collected at 40 mV s^{-1} in 1.0 M, pH 9.6 potassium borate buffer electrolyte.

4.3.2. H_2 Evolution Measurement by Gas Chromatography

The photocatalytic hydrogen evolution experiments are carried out using a xenon arc lamp equipped with a 400 nm long pass filter, and the illumination intensity is calibrated to 1 sun. No sacrificial reagent is used. The test sample is prepared by diluting the photocatalyst stock solution in 0.1 M potassium borate buffer to set the optical density at 705 nm to 1 with 1 cm pathlength. 5 mL of the sample is loaded to a 25 mL septum-sealed three-neck round bottom flask. Prior to irradiation, the suspension is sonicated for 10 minutes and is deaerated by bubbling argon gas (99.999% ultra-high purity) through the sample solution for 30 minutes. Then the sample solution is irradiated for 2 hrs under the xenon lamp to allow H_2 accumulation in the head space of the flask. Following the irradiation, 10 mL of the gas in the headspace is injected to a gas chromatography analyzer (SRI model 8610C) equipped with a molecular sieve column and a thermal conductivity detector (TCD) using argon carrier gas. For the TCD to detect significant amount of H_2, it is necessary here to accumulate H_2 for a prolonged time period and use a larger amount of sample than the case for Clark electrode measurement. The absolute concentration of hydrogen produces in the headspace, c_{H2}, is quantified with a calibration curve generated by measuring a series of Ar gas samples dosed with known concentrations of H_2. The mass efficiencies of H_2 production (ME_{H2}, $mmolh^{-1}g^{-1}$) are calculated by the following equations, where n_{H2} is the amount of produced H_2 in the headspace at 20 °C (T) and 1 atm (P), V_{head} is the headspace volume (41 mL), m_{cat} is the mass of the photocatalyst used (94.7 μg), and t is the illumination time (2 hours).

$$n_{H2} = \frac{P \times V_{head}}{RT} \times c_{H2} \qquad (5)$$

$$ME_{H2} = \frac{n_{H2}}{m_{cat} \times t} \qquad (6)$$

In Fig. 4.7, the photocatalytic HER performance of the integrated photocatalyst is compared with that of its precursors missing individual components. The H_2 evolution rates of Au/TiO_2 and $Au/TiO_2/CoO_x$ nanostructures are within the measurement error and can be considered as negligible. The full structure produces c_{H2} of 48.8 ± 6.05 ppm which corresponds to the HER rate of 0.42 ± 0.05 $mmolg^{-1}h^{-1}$. The $Au/TiO_2/CoO_x/Pd$ nanostructure produces c_{H2} of 16.3 ± 10.0 ppm which corresponds lower HER rate of 0.14 ± 0.09 $mmolg^{-1}h^{-1}$ measured for $Au/TiO_2/CoO_x/Pd$ nanostructure. The trend of HER activities for the series of nanostructures studied here matches well with trend of the *in situ* O_2 measurement data. However, the absolute rate of HER cannot be directly compared to the absolute rate of OER measured by the Clark electrode with the 2:1 stoichiometric ratio, due to the different factors such as the illumination geometry and experimental timescales.

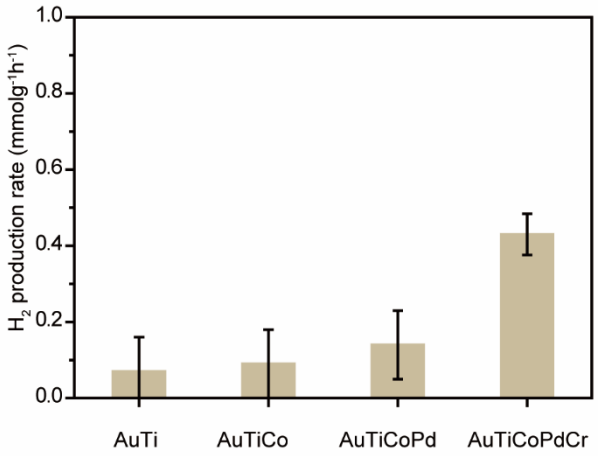

Figure 4.7. Comparison of the H_2 evolution rates of various nanostructures.

4.3.3. Mechanism of the Full Water Splitting by Plasmonic Resonance

To verify the proposed charge transfer pathway in Fig. 4.1b, we apply optical filters and compare the photocatalytic performance to the white light excitation condition. Three optical pass filters are used to selectively excite the interband and LSPR transitions: a 400 nm long pass filter, a 560 nm long pass filter, and a 530 short pass filter. The transmittance spectrum of each filter is shown in Fig. 4.8. Only the LSPR transition would be excited when the 400 nm long-pass and the 560 nm long-pass filters are used jointly; only the interband transition would be excited when the 400 nm long-pass and the 530 nm short-pass filters are used jointly. When the 400 nm long pass filter and the 530 nm short pass filter are used jointly, the Xe lamp intensity is adjusted due to the spectrum loss of the short pass filter in the range of 400 nm < λ < 530 nm. The lamp intensity is adjusted to account for the optical loss of filters and maintain the spectral density of different excitation wavelengths at the AM 1.5G level with different filter sets.

No oxygen production is observed in Fig. 4.9 when only one of the two transitions is excited. This is also confirmed by the photocatalytic HER activity profile as shown in Fig. 4.10. This phenomenon indicates that the LSPR and the interband transition each is responsible only for a half reaction. The full water splitting reaction cannot proceed when either of the half reactions was turned off. It had been demonstrated previously that the LSPR transitions could drive HER half reaction.[73]

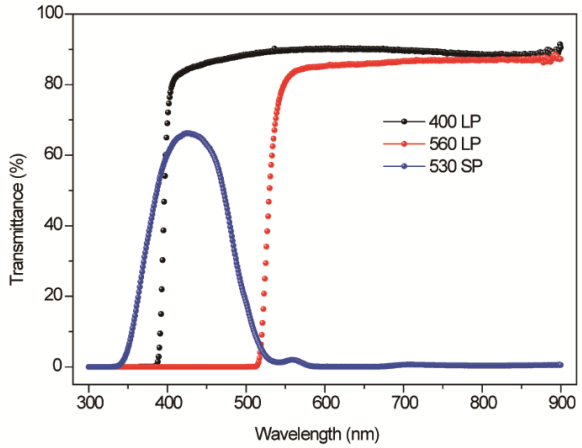

Figure 4.8. Transmittance spectrum of different pass filters: 400 nm long pass filter (black), 560 nm long pass filter (red), and 530 nm short pass filter (blue).

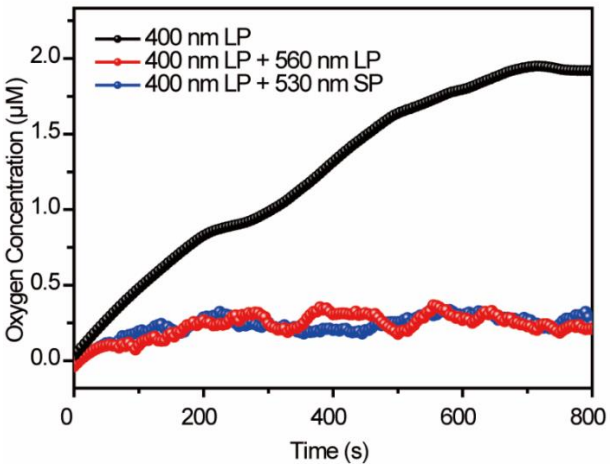

Figure 4.9. The photocatalytic OER performance of the $Au/TiO_2/CoO_x/Pd/Cr_2O_3$ nanostructure with different optical filters applied.

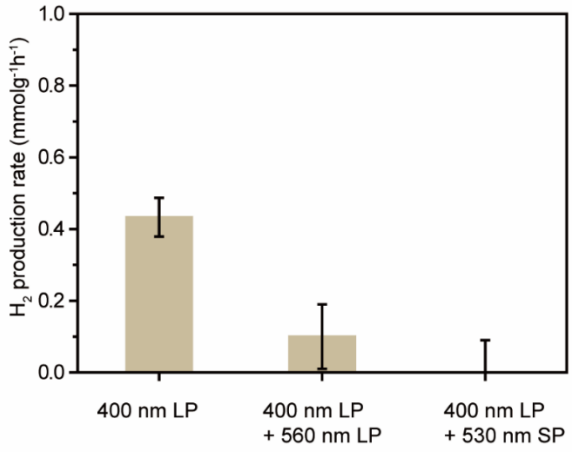

Figure 4.10. The photocatalytic HER performance of the $Au/TiO_2/CoO_x/Pd/Cr_2O_3$ nanostructure with different optical filters applied.

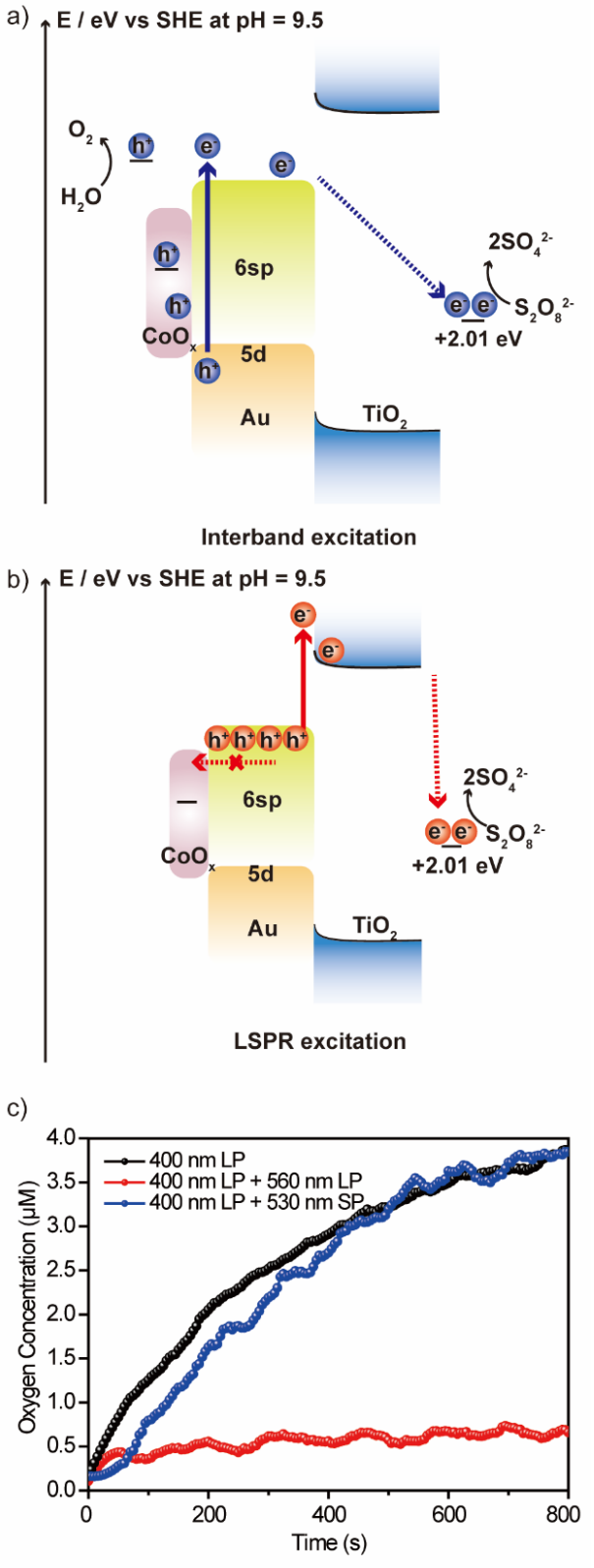

Figure 4.11. a,b) Schematic energy diagrams of the Au/TiO_2/CoO_x nanostructure under interband (a) or LSPR (b) excitations when sodium persulfate was added as the electron scavenger. c) OER performance of the Au/TiO_2/CoOx nanostructure under different excitation conditions.

The proposed mechanism of OER half reaction using a sacrificial electron acceptor is depicted in Fig. 4.11a and Fig. 4.11b. Whereas both electrons at Fermi level of Au and at the conduction band of TiO_2 can reduce the persulfate anions, exciting LSPR transition would not produce oxygen since this process does not create deep holes transferrable to CoO_x. In Fig. 4.11c, the *in situ* O_2 evolution performance is analyzed with 0.1 M sodium persulfate using $Au/TiO_2/CoO_x$ nanostructures. The lamp intensity is adjusted to account for the optical loss of filters and maintain the spectral density of different excitation wavelengths at the AM 1.5G level with different filter sets. As expected, excitation with 560 nm long pass filter results with negligible O_2 production, whereas the O_2 production rate of the excitation with 530 nm short pass filter almost fully matches that of the white light excitation. Though the excitation condition with 560 nm long pass filter can involve a minor contribution from the *d-sp* transition, the clear absence of OER activity proves that the tail of *d-sp* transition has negligible photocatalytic effects, and thus will not alter the indication that the longitudinal LSPR mode does not contribute significantly to OER activity in the integrated photocatalyst.

4.3.4. Photostability Measurement of Synthesized Photocatalyst

In Fig. 4.12, the HER activity of $Au/TiO_2/CoO_x/Pd/Cr_2O_3$ in 0.1 M potassium borate buffer without using scavengers is evaluated for several 2-hour illumination cycles under the intensity of 1 sun. The HER rates of three consecutive cycles are 0.5 $mmolg^{-1}hr^{-1}$, 0.4 $mmolg^{-1}hr^{-1}$ and 0.38 $mmolg^{-1}hr^{-1}$, respectively. There is only minor decrease in photocatalytic activity during total period of 6 hrs. As shown in Fig. 4.13, HR-TEM analysis and UV-vis spectroscopy are used to characterize the photocatalysts before and after illumination. The TEM images indicate no apparent structural change of the particles. The UV-vis spectrum of the integrated photocatalyst shows no broadening or peak-shift. A minor absorbance change of the UV-vis spectrum is due to the attachment of particles on the wall of the reactor.

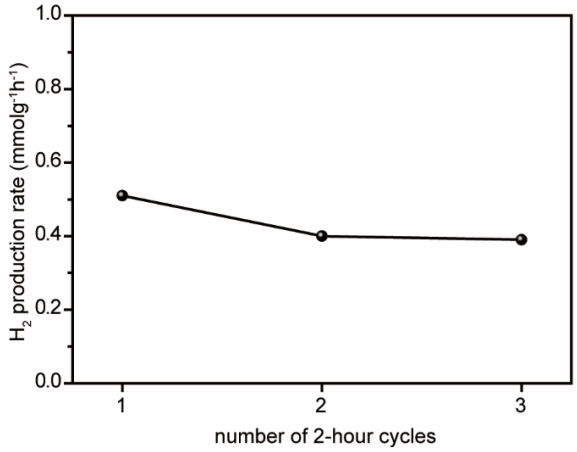

Figure 4.12. The photocatalytic activity of H_2 evolution reaction measured for several 2-hour periods using $Au/TiO_2/CoO_x/Pd/Cr_2O_3$ nanostructure. Each datapoint was recorded by measuring the accumulated H_2 gas after 2 hrs of simulated solar irradiation.

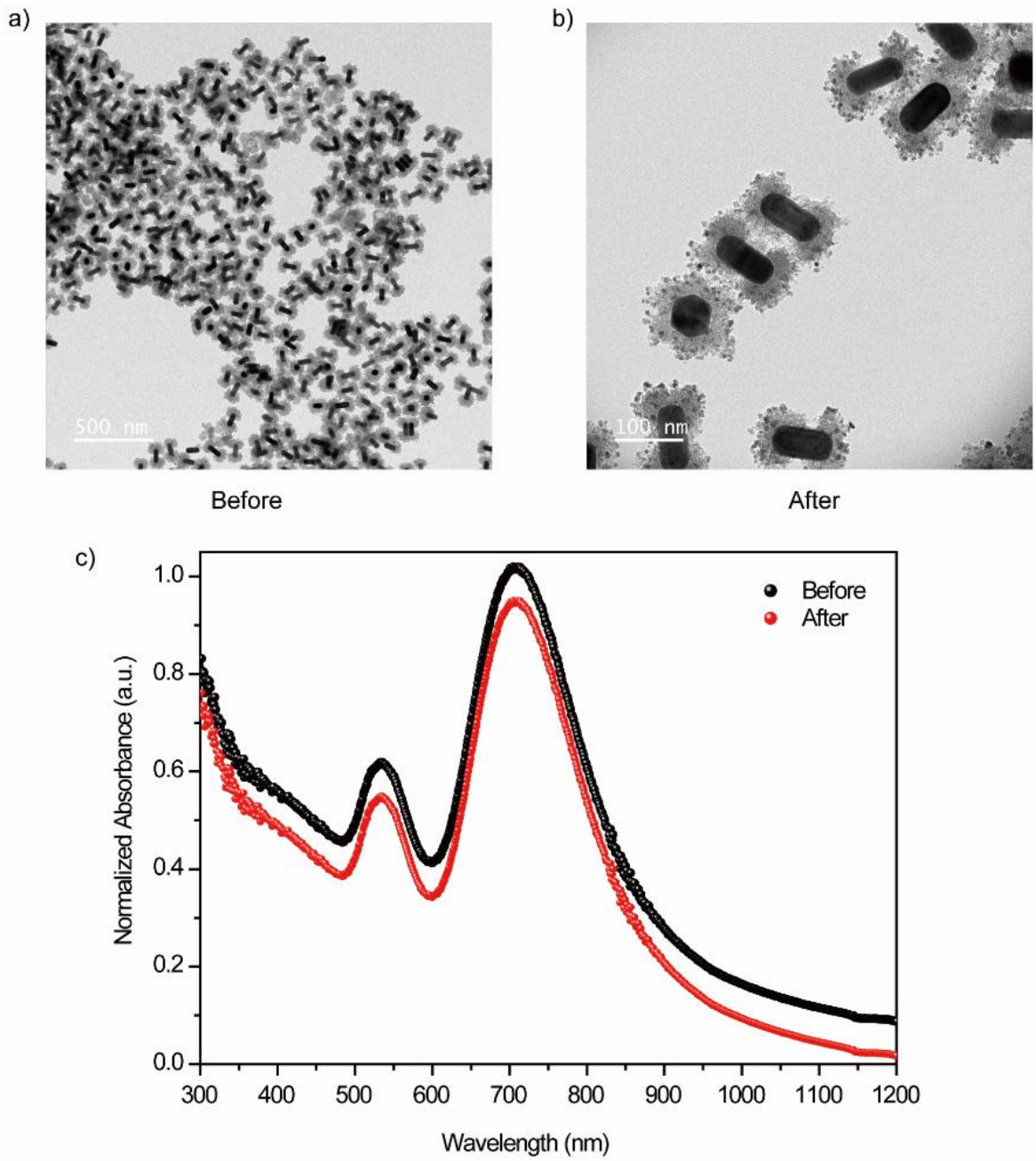

Figure 4.13. Photostability test. HR-TEM images before a), and after b) 6 hrs photochemical test with 1 sun irradiation in 0.1 M potassium borate buffer c) The absorption spectrum before and after irradiation.

4.4 Conclusion

It is rare for a single optical absorption band to possess the suitable energy levels to drive both the HER and OER while covering well the solar wavelength range.[62] Natural and artificial photosynthetic systems often contain multiple absorbers in the HER and OER units working in tandem to drive the overall reaction. Our results here suggest that the charge carriers generated from the longitudinal LSPR and the interband transitions in the same nanoparticle work in tandem to achieve a full water splitting reaction. This mechanism does not imply that the photocatalyst requires a simultaneous two-photon absorption exciting both the longitudinal LSPR and interband transitions to function. The charge carriers from different transitions can flow tandemly as long as the charge separation lifetime is sufficiently long to accumulate charges between sequential photoexcitation events.

Chapter 5. Conclusion and Future Direction

In this dissertation, light-induced synthesis of polyelemental nanoparticle via redox chemistry have been introduced. To provide charge separated regions in a single nanoparticle, anisotropic shape of nanoparticle needs to be a basic building block. Here, gold nanorods which have different charge distribution at the end and side, have interesting plasmonic property which can harvest hot charge carriers in visible-IR regions of the sun spectrum, and TiO_2 can capture the hot electrons transferred by AuNR. Thus, Au/TiO_2 nanodumbbell structure have been used as a platform for the library of various polyelemental nanoparticles. By tuning different light source and scavengers, site-selective photodeposition of either metal or metal oxide has been realized. Such a complex system including reduction and oxidation sites has been further applied to the full water splitting reaction with five necessary components to improve the photocatalytic performance. The mechanism of the photocatalytic reaction has been demonstrated that the hot charge carriers from exciting both d-sp interband transition and the LSPR of AuNR are required to drive the full water splitting reaction.

For future work, transient absorption measurements can be carried out to directly track the charge transfer pathway in the integrated system. The multiple interfaces between different material components can potentially generate charge trapping sites which are not well characterized within the scope of this work. Improved junction designs at the Au/CoOx and Au/TiO_2 interfaces can be crucial for further enhancing the hot carrier harvesting efficiency. The solution phase photoredox deposition strategy demonstrated here can be used to precisely fabricate complex inorganic colloidal building blocks and assemblies with potential applications in energy harvesting, catalysis, plasmonics, and nanoelectronics.

References

(1) Nasrollahzadeh, M.; Sajjadi, M.; Iravani, S.; Varma, R. S. Trimetallic Nanoparticles: Greener Synthesis and Their Applications. *Nanomaterials*, **2020**, *10 (9)*, 1784.

(2) Chen, P.-C.; Liu, M.; Du, J. S.; Meckes, B.; Wang, S.; Lin, H.; Dravid, V. P.; Wolverton, C.; Mirkin, C. A. Interface and Heterostructure Design in Polyelemental Nanoparticles. *Science* **2019**, *363* (6430), 959 – 964.

(3) Yang, H.; Bradley, S. J.; Wu, X.; Chan, A.; Waterhouse, G. I. N.; Nann, T.; Zhang, J.; Kruger, P. E.; Ma, S.; Telfer, S. G. General Synthetic Strategy for Libraries of Supported Multicomponent Metal Nanoparticles. *ACS Nano* **2018**, *12* (5), 4594–4604.

(4) Chen, P.-C.; Liu, G.; Zhou, Y.; Brown, K. A.; Chernyak, N.; Hedrick, J. L.; He, S.; Xie, Z.; Lin, Q.-Y.; Dravid, V. P.; O'Neill-Slawecki, S. A.; Mirkin, C. A. Tip-Directed Synthesis of Multimetallic Nanoparticles. *J. Am. Chem. Soc.* **2015**, *137* (28), 9167–9173..

(5) Singh, A. K.; Xu, Q. Synergistic Catalysis over Bimetallic Alloy Nanoparticles. *ChemCatChem* **2013**, *5* (3), 652–676.

(6) Yao, Y.; Huang, Z.; Li, T.; Wang, H.; Liu, Y.; Stein, H. S.; Mao, Y.; Gao, J.; Jiao, M.; Dong, Q.; Dai, J.; Xie, P.; Xie, H.; Lacey, S. D.; Takeuchi, I.; Gregoire, J. M.; Jiang, R.; Wang, C.; Taylor, A. D.; Shahbazian-Yassar, R.; Hu, L. High-Throughput, Combinatorial Synthesis of Multimetallic Nanoclusters. *Proc. Natl. Acad. Sci.* **2020**, *117* (12), 6316 – 6322.

(7) Croce, R.; Van Amerongen, H. Natural Strategies for Photosynthetic Light Harvesting. *Nat. Chem. Biol.* **2014**, *10* (7), 492–501.

(8) Khan, I.; Saeed, K.; Khan, I. Nanoparticles: Properties, Applications and Toxicities. *Arab. J. Chem.* **2019**, *12* (7), 908–931.

(9) Faraday, M. X. The Bakerian Lecture. —Experimental Relations of Gold (and Other Metals) to Light. *Philos. Trans. R. Soc. London* **1857**, *147*, 145–181.

(10) Yu, H.; Peng, Y.; Yang, Y.; Li, Z.-Y. Plasmon-Enhanced Light–Matter Interactions and Applications. *npj Comput. Mater.* **2019**, *5* (1), 45.

(11) Biagioni, P.; Huang, J.-S.; Hecht, B. Nanoantennas for Visible and Infrared Radiation. *Reports Prog. Phys.* **2012**, *75* (2), 24402.

(12) Matthew, Pelton; Garnett, B. *Introduction to Metal-Nanoparticle Plasmonics*; John Wiley & Sons, Ltd: New Jersey, **2013**.

(13) Olson, J.; Dominguez-Medina, S.; Hoggard, A.; Wang, L.-Y.; Chang, W.-S.; Link, S. Optical Characterization of Single Plasmonic Nanoparticles. *Chem. Soc. Rev.* **2015**, *44* (1), 40–57.

(14) Clavero, C. Plasmon-Induced Hot-Electron Generation at Nanoparticle/Metal-

Oxide Interfaces for Photovoltaic and Photocatalytic Devices. *Nat. Photonics* **2014**, *8* (2), 95–103.

(15) Seh, Z. W.; Liu, S.; Low, M.; Zhang, S.-Y.; Liu, Z.; Mlayah, A.; Han, M.-Y. Janus Au-TiO_2 Photocatalysts with Strong Localization of Plasmonic Near-Fields for Efficient Visible-Light Hydrogen Generation. *Adv. Mater.* **2012**, *24* (17), 2310–2314.

(16) Seh, Z. W.; Liu, S.; Zhang, S.-Y.; Bharathi, M. S.; Ramanarayan, H.; Low, M.; Shah, K. W.; Zhang, Y.-W.; Han, M.-Y. Anisotropic Growth of Titania onto Various Gold Nanostructures: Synthesis, Theoretical Understanding, and Optimization for Catalysis. *Angew. Chem. Int. Ed.* **2011**, *123* (43), 10322–10325.

(17) Grzelczak, M.; Pérez-Juste, J.; Mulvaney, P.; Liz-Marzán, L. M. Shape Control in Gold Nanoparticle Synthesis. *Chem. Soc. Rev.* **2008**, *37* (9), 1783–1791.

(18) Langille, M. R.; Personick, M. L.; Zhang, J.; Mirkin, C. A. Defining Rules for the Shape Evolution of Gold Nanoparticles. *J. Am. Chem. Soc.* **2012**, *134* (35), 14542–14554.

(19) Glasscott, M. W.; Pendergast, A. D.; Goines, S.; Bishop, A. R.; Hoang, A. T.; Renault, C.; Dick, J. E. Electrosynthesis of High-Entropy Metallic Glass Nanoparticles for Designer, Multi-Functional Electrocatalysis. *Nat. Commun.* **2019**, *10* (1), 2650.

(20) Chen, P.-C.; Liu, X.; Hedrick, J. L.; Xie, Z.; Wang, S.; Lin, Q.-Y.; Hersam, M. C.; Dravid, V. P.; Mirkin, C. A. Polyelemental Nanoparticle Libraries. *Science* **2016**, *352* (6293), 1565 – 1569.

(21) Yao, Y.; Huang, Z.; Xie, P.; Lacey, S. D.; Jacob, R. J.; Xie, H.; Chen, F.; Nie, A.; Pu, T.; Rehwoldt, M.; Yu, D.; Zachariah, M. R.; Wang, C.; Shahbazian-Yassar, R.; Li, J.; Hu, L. Carbothermal Shock Synthesis of High-Entropy-Alloy Nanoparticles. *Science* **2018**, *359* (6383), 1489 – 1494.

(22) Wenderich, K.; Mul, G. Methods, Mechanism, and Applications of Photodeposition in Photocatalysis: A Review. *Chem. Rev.* **2016**, *116* (23), 14587–14619.

(23) Ye, X.; Zheng, C.; Chen, J.; Gao, Y.; Murray, C. B. Using Binary Surfactant Mixtures To Simultaneously Improve the Dimensional Tunability and Monodispersity in the Seeded Growth of Gold Nanorods. *Nano Lett.* **2013**, *13* (2), 765–771.

(24) Wu, B.; Liu, D.; Mubeen, S.; Chuong, T. T.; Moskovits, M.; Stucky, G. D. Anisotropic Growth of TiO2 onto Gold Nanorods for Plasmon-Enhanced Hydrogen Production from Water Reduction. *J. Am. Chem. Soc.* **2016**, *138* (4), 1114–1117.

(25) Knight, M. W.; Sobhani, H.; Nordlander, P.; Halas, N. J. Photodetection with

Active Optical Antennas. *Science* **2011**, *332* (6030), 702 – 704.

(26) Drummond, T. J. Work Functions of the Transition Metals and Metal Silicides. **1999**.

(27) Ayati, A.; Ahmadpour, A.; Bamoharram, F. F.; Tanhaei, B.; Mänttäri, M.; Sillanpää, M. A Review on Catalytic Applications of Au/TiO_2 Nanoparticles in the Removal of Water Pollutant. *Chemosphere* **2014**, *107*, 163–174.

(28) Zhong, D. K.; Gamelin, D. R. Photo-Electrochemical Water Oxidation by Cobalt Catalyst ("Co-Pi")/α-Fe_2O_3 Composite Photoanodes: Oxygen Evolution and Resolution of a Kinetic Bottleneck. *J. Am. Chem. Soc.* **2010**, *132* (12), 4202–4207.

(29) Mattioli, G.; Giannozzi, P.; Amore Bonapasta, A.; Guidoni, L. Reaction Pathways for Oxygen Evolution Promoted by Cobalt Catalyst. *J. Am. Chem. Soc.* **2013**, *135* (41), 15353–15363.

(30) Surendranath, Y.; Kanan, M. W.; Nocera, D. G. Mechanistic Studies of the Oxygen Evolution Reaction by a Cobalt-Phosphate Catalyst at Neutral pH. *J. Am. Chem. Soc.* **2010**, *132* (46), 16501–16509.

(31) Francàs, L.; Corby, S.; Selim, S.; Lee, D.; Mesa, C. A.; Godin, R.; Pastor, E.; Stephens, I. E. L.; Choi, K.-S.; Durrant, J. R. Spectroelectrochemical Study of Water Oxidation on Nickel and Iron Oxyhydroxide Electrocatalysts. *Nat. Commun.* **2019**, *10* (1), 5208.

(32) Suryanto, B. H. R.; Wang, Y.; Hocking, R. K.; Adamson, W.; Zhao, C. Overall Electrochemical Splitting of Water at the Heterogeneous Interface of Nickel and Iron Oxide. *Nat. Commun.* **2019**, *10* (1), 5599.

(33) Davis, S. J.; Lewis, N. S.; Shaner, M.; Aggarwal, S.; Arent, D.; Azevedo, I. L.; Benson, S. M.; Bradley, T.; Brouwer, J.; Chiang, Y.-M.; Clack, C. T. M.; Cohen, A.; Doig, S.; Edmonds, J.; Fennell, P.; Field, C. B.; Hannegan, B.; Hodge, B.-M.; Hoffert, M. I.; Ingersoll, E.; Jaramillo, P.; Lackner, K. S.; Mach, K. J.; Mastrandrea, M.; Ogden, J.; Peterson, P. F.; Sanchez, D. L.; Sperling, D.; Stagner, J.; Trancik, J. E.; Yang, C.-J.; Caldeira, K. Net-Zero Emissions Energy Systems. *Science* **2018**, *360* (6396), eaas9793.

(34) Lewis, N. S.; Nocera, D. G. Powering the Planet: Chemical Challenges in Solar Energy Utilization. *Proc. Natl. Acad. Sci.* **2006**, *103* (43), 15729 – 15735.

(35) Jiang, C.; Moniz, S. J. A.; Wang, A.; Zhang, T.; Tang, J. Photoelectrochemical Devices for Solar Water Splitting – Materials and Challenges. *Chem. Soc. Rev.* **2017**, *46* (15), 4645–4660.

(36) Liu, C.; Tang, J.; Chen, H. M.; Liu, B.; Yang, P. A Fully Integrated Nanosystem of Semiconductor Nanowires for Direct Solar Water Splitting. *Nano Lett.* **2013**, *13* (6), 2989–2992.

(37) Edri, E.; Cooper, J. K.; Sharp, I. D.; Guldi, D. M.; Frei, H. Ultrafast Charge

Transfer between Light Absorber and Co_3O_4 Water Oxidation Catalyst across Molecular Wires Embedded in Silica Membrane. *J. Am. Chem. Soc.* **2017**, *139* (15), 5458–5466.

(38) DuChene, J. S.; Tagliabue, G.; Welch, A. J.; Cheng, W.-H.; Atwater, H. A. Hot Hole Collection and Photoelectrochemical CO_2 Reduction with Plasmonic Au/p-GaN Photocathodes. *Nano Lett.* **2018**, *18* (4), 2545–2550.

(39) Mubeen, S.; Lee, J.; Singh, N.; Krämer, S.; Stucky, G. D.; Moskovits, M. An Autonomous Photosynthetic Device in Which All Charge Carriers Derive from Surface Plasmons. *Nat. Nanotechnol.* **2013**, *8* (4), 247–251.

(40) Cestellos-Blanco, S.; Zhang, H.; Kim, J. M.; Shen, Y.; Yang, P. Photosynthetic Semiconductor Biohybrids for Solar-Driven Biocatalysis. *Nat. Catal.* **2020**, *3* (3), 245–255.

(41) Zhang, J. Z.; Reisner, E. Advancing Photosystem II Photoelectrochemistry for Semi-Artificial Photosynthesis. *Nat. Rev. Chem.* **2020**, *4* (1), 6–21.

(42) Croce, R.; van Amerongen, H. Natural Strategies for Photosynthetic Light Harvesting. *Nat. Chem. Biol.* **2014**, *10* (7), 492–501.

(43) Oh, M. H.; Cho, M. G.; Chung, D. Y.; Park, I.; Kwon, Y. P.; Ophus, C.; Kim, D.; Kim, M. G.; Jeong, B.; Gu, X. W.; Jo, J.; Yoo, J. M.; Hong, J.; McMains, S.; Kang, K.; Sung, Y.-E.; Alivisatos, A. P.; Hyeon, T. Design and Synthesis of Multigrain Nanocrystals via Geometric Misfit Strain. *Nature* **2020**, *577* (7790), 359–363.

(44) Steimle, B. C.; Fenton, J. L.; Schaak, R. E. Rational Construction of a Scalable Heterostructured Nanorod Megalibrary. *Science* **2020**, *367* (6476), 418 – 424.

(45) Ding, D.; Liu, K.; He, S.; Gao, C.; Yin, Y. Ligand-Exchange Assisted Formation of Au/TiO_2 Schottky Contact for Visible-Light Photocatalysis. *Nano Lett.* **2014**, *14* (11), 6731–6736.

(46) Kalisman, P.; Nakibli, Y.; Amirav, L. Perfect Photon-to-Hydrogen Conversion Efficiency. *Nano Lett.* **2016**, *16* (3), 1776–1781.

(47) Zheng, Z.; Tachikawa, T.; Majima, T. Single-Particle Study of Pt-Modified Au Nanorods for Plasmon-Enhanced Hydrogen Generation in Visible to Near-Infrared Region. *J. Am. Chem. Soc.* **2014**, *136* (19), 6870–6873.

(48) Zhu, M.; Wang, Y.; Deng, Y.-H.; Peng, X.; Wang, X.; Yuan, H.; Yang, Z.-J.; Wang, Y.; Wang, H. Strategic Modulation of Energy Transfer in Au-TiO_2-Pt Nanodumbbells: Plasmon-Enhanced Hydrogen Evolution Reaction. *Nanoscale* **2020**, *12* (13), 7035–7044..

(49) Ben-Shahar, Y.; Scotognella, F.; Kriegel, I.; Moretti, L.; Cerullo, G.; Rabani, E.; Banin, U. Optimal Metal Domain Size for Photocatalysis with Hybrid Semiconductor-Metal Nanorods. *Nat. Commun.* **2016**, *7* (1), 10413.

(50) Kalisman, P.; Kauffmann, Y.; Amirav, L. Photochemical Oxidation on Nanorod Photocatalysts. *J. Mater. Chem. A* **2015**, *3* (7), 3261–3265.

(51) Dukovic, G.; Merkle, M. G.; Nelson, J. H.; Hughes, S. M.; Alivisatos, A. P. Photodeposition of Pt on Colloidal CdS and CdSe/CdS Semiconductor Nanostructures. *Adv. Mater.* **2008**, *20* (22), 4306–4311.

(52) Elbanna, O.; Kim, S.; Fujitsuka, M.; Majima, T. TiO_2 Mesocrystals Composited with Gold Nanorods for Highly Efficient Visible-NIR-Photocatalytic Hydrogen Production. *Nano Energy* **2017**, *35*, 1–8.

(53) Qian, K.; Sweeny, B. C.; Johnston-Peck, A. C.; Niu, W.; Graham, J. O.; DuChene, J. S.; Qiu, J.; Wang, Y.-C.; Engelhard, M. H.; Su, D.; Stach, E. A.; Wei, W. D. Surface Plasmon-Driven Water Reduction: Gold Nanoparticle Size Matters. *J. Am. Chem. Soc.* **2014**, *136* (28), 9842–9845.

(54) DuChene, J. S.; Sweeny, B. C.; Johnston-Peck, A. C.; Su, D.; Stach, E. A.; Wei, W. D. Prolonged Hot Electron Dynamics in Plasmonic-Metal/Semiconductor Heterostructures with Implications for Solar Photocatalysis. *Angew. Chem. Int. Ed.* **2014**, *53* (30), 7887–7891.

(55) Brongersma, M. L.; Halas, N. J.; Nordlander, P. Plasmon-Induced Hot Carrier Science and Technology. *Nat. Nanotechnol.* **2015**, *10* (1), 25–34.

(56) Halas, N. J.; Lal, S.; Chang, W.-S.; Link, S.; Nordlander, P. Plasmons in Strongly Coupled Metallic Nanostructures. *Chem. Rev.* **2011**, *111* (6), 3913–3961.

(57) Winsemius, P.; Guerrisi, M.; Rosei, R. Splitting of the Interband Absorption Edge in Au: Temperature Dependence. *Phys. Rev. B* **1975**, *12* (10), 4570–4572.

(58) Bernardi, M.; Mustafa, J.; Neaton, J. B.; Louie, S. G. Theory and Computation of Hot Carriers Generated by Surface Plasmon Polaritons in Noble Metals. *Nat. Commun.* **2015**, *6* (1), 7044.

(59) Zhao, J.; Nguyen, S. C.; Ye, R.; Ye, B.; Weller, H.; Somorjai, G. A.; Alivisatos, A. P.; Toste, F. D. A Comparison of Photocatalytic Activities of Gold Nanoparticles Following Plasmonic and Interband Excitation and a Strategy for Harnessing Interband Hot Carriers for Solution Phase Photocatalysis. *ACS Cent. Sci.* **2017**, *3* (5), 482–488.

(60) Kim, Y.; Smith, J. G.; Jain, P. K. Harvesting Multiple Electron–Hole Pairs Generated through Plasmonic Excitation of Au Nanoparticles. *Nat. Chem.* **2018**, *10* (7), 763–769.

(61) Zou, N.; Chen, G.; Mao, X.; Shen, H.; Choudhary, E.; Zhou, X.; Chen, P. Imaging Catalytic Hotspots on Single Plasmonic Nanostructures via Correlated Super-Resolution and Electron Microscopy. *ACS Nano* **2018**, *12* (6), 5570–5579.

(62) Ng, B.-J.; Putri, L. K.; Kong, X. Y.; Teh, Y. W.; Pasbakhsh, P.; Chai, S.-P. Z-

Scheme Photocatalytic Systems for Solar Water Splitting. *Adv. Sci.* **2020**, *7* (7), 1903171.

(63) Lee, J.; Mubeen, S.; Ji, X.; Stucky, G. D.; Moskovits, M. Plasmonic Photoanodes for Solar Water Splitting with Visible Light. *Nano Lett.* **2012**, *12* (9), 5014–5019.

(64) Nishi, H.; Tatsuma, T. Mechanistic Analysis of Plasmon-Induced Charge Separation by the Use of Chemically Synthesized Gold Nanorods. *J. Phys. Chem. C* **2018**, *122* (4), 2330–2335.

(65) Schoenlein, R. W.; Lin, W. Z.; Fujimoto, J. G.; Eesley, G. L. Femtosecond Studies of Nonequilibrium Electronic Processes in Metals. *Phys. Rev. Lett.* **1987**, *58* (16), 1680–1683.

(66) Liu, H.; Frei, H. Observation of O–O Bond Forming Step of Molecular Co_4O_4 Cubane Catalyst for Water Oxidation by Rapid-Scan FT-IR Spectroscopy. *ACS Catal.* **2020**, *10* (3), 2138–2147.

(67) Materna, K. L.; Jiang, J.; Regan, K. P.; Schmuttenmaer, C. A.; Crabtree, R. H.; Brudvig, G. W. Optimization of Photoanodes for Photocatalytic Water Oxidation by Combining a Heterogenized Iridium Water-Oxidation Catalyst with a High-Potential Porphyrin Photosensitizer. *ChemSusChem* **2017**, *10* (22), 4526–4534.

(68) Li, J.-X.; Ye, C.; Li, X.-B.; Li, Z.-J.; Gao, X.-W.; Chen, B.; Tung, C.-H.; Wu, L.-Z. A Redox Shuttle Accelerates O_2 Evolution of Photocatalysts Formed In Situ under Visible Light. *Adv. Mater.* **2017**, *29* (17), 1606009.

(69) Park, K.; Biswas, S.; Kanel, S.; Nepal, D.; Vaia, R. A. Engineering the Optical Properties of Gold Nanorods: Independent Tuning of Surface Plasmon Energy, Extinction Coefficient, and Scattering Cross Section. *J. Phys. Chem. C* **2014**, *118* (11), 5918–5926.

(70) Yoshida, M.; Takanabe, K.; Maeda, K.; Ishikawa, A.; Kubota, J.; Sakata, Y.; Ikezawa, Y.; Domen, K. Role and Function of Noble-Metal/Cr-Layer Core/Shell Structure Cocatalysts for Photocatalytic Overall Water Splitting Studied by Model Electrodes. *J. Phys. Chem. C* **2009**, *113* (23), 10151–10157.

(71) Maeda, K.; Teramura, K.; Lu, D.; Saito, N.; Inoue, Y.; Domen, K. Noble-Metal/Cr_2O_3 Core/Shell Nanoparticles as a Cocatalyst for Photocatalytic Overall Water Splitting. *Angew. Chemie Int. Ed.* **2006**, *45* (46), 7806–7809.

(72) Takata, T.; Jiang, J.; Sakata, Y.; Nakabayashi, M.; Shibata, N.; Nandal, V.; Seki, K.; Hisatomi, T.; Domen, K. Photocatalytic Water Splitting with a Quantum Efficiency of Almost Unity. *Nature* **2020**, *581* (7809), 411–414.

(73) Duchene, J. S.; Sweeny, B. C.; Johnston-Peck, A. C.; Su, D.; Stach, E. A.; Wei, W. D. Prolonged Hot Electron Dynamics in Plasmonic-Metal/Semiconductor Heterostructures with Implications for Solar Photocatalysis. *Angew. Chem. Int.*

Ed. **2014**, *53* (30), 7887–7891.

(74) Zheng, Y.; Zhong, X.; Li, Z.; Xia, Y. Successive, Seed-Mediated Growth for the Synthesis of Single-Crystal Gold Nanospheres with Uniform Diameters Controlled in the Range of 5–150 nm. *Part. Part. Syst. Charact.* **2014**, *31* (2), 266–273.

Appendix 1. Materials

Syntheses were carried out using commercially purchased reagents without further purification. Hexadecyltrimethylammonium bromide (CTAB, >98.0%), hexadecyltrimethylammonium chloride (CTAC, >95.0%), and sodium oleate (NaOL, >97.0%) were purchased from TCI America. Isopropanol (IPA, 99.5%), sodium bicarbonate ($NaHCO_3$) was purchased from EMD Milipore. Titanium chloride ($TiCl_3$, 20% w/v solution in 2N hydrochloric acid) was obtained from Fisher Scientific. Hydrogen tetrachloroaurate trihydrate ($HAuCl_4 \cdot 3H_2O$, ≥99.9%), L-ascorbic acid (BioXtra, ≥99.0%), silver nitrate ($AgNO_3$, ≥99.0%), sodium borohydride ($NaBH_4$, 99.99%), hydrochloric acid (36.5%-38.0% wt%), sodium bicarbonate, cobalt nitrate hexahydrate ($Co(NO_3)_2 \cdot 6H_2O$, 99.0%), sodium persulfate ($Na_2S_2O_8$, ≥99.0%), palladium chloride ($PdCl_2$, 99%), anhydrous methanol (99%), boric acid (H_3BO_3, ≥99.5%), potassium hydroxide (KOH, ≥85.0%), potassium hexachloroplatinate (K_2PtCl_6, 98%), copper nitrate trihydrate ($Cu(NO_3)_2 \cdot 3H_2O$, 99%), iron sulfate heptahydrate ($FeSO_4 \cdot 3H_2O$, ≥99.9%), potassium sulfate (K_2SO_4, ≥99.0%) hydroxypropyl cellulose (M_w = 370,000), titanium diisopropoxide bis(acetylacetonate) (75 wt. % in isopropanol), poly(ethylene glycol) methyl ether thiol (average M_n = 6,000), ammonia solution (2.0M in isopropanol), and potassium chromate (K_2CrO_4, ≥99.0%), were purchased from Sigma Aldrich (USA). $NaBH_4$ powder was stored in an argon glovebox. $TiCl_3$, $HAuCl_4 \cdot 3H_2O$, L-ascorbic acid, and $AgNO_3$ were stored in a vacuum desiccator at room temperature. Deionized water (DI-water, Milipore, Milford, MA, USA) was used for all aqueous solution. All the glassware was thoroughly cleaned using freshly prepared aqua regia (3:1 volume ratio of HCl and HNO_3, respectively) followed by fully rinsing with copious amount of DI-water.

Appendix 2. Synthesis of Janus-typed TiO_2 Capped Au Nanosphere

A.2.1 Synthesis of CTAC Capped Au Nanosphere

Highly uniform 80 nm size of Au nanospheres are prepared by a successive, seed-mediated method.[74]

Seed preparation*:* 10 mL of 0.1 M CTAB solution was mixed with 100 μL of 25 mM $HAuCl_4$ in a 20 mL scintillation vial under vigorous stirring. 600 μL of ice cooled 10 mM $NaBH_4$ was rapidly injected into the Au-CTAB solution and stirred for 2 min. Upon the addition of $NaBH_4$, the color of the seed solution turned yellow-brownish. Afterward, the seed solution was left undisturbed at 28 ^oC for 30 min prior to use in the following step.

10 nm sized Au nanosphere preparation*:* 6 mL of 0.2 M CTAC solution was mixed with 150 μL of the seed solution. 4.5 mL of 0.1 M ascorbic acid solution is injected into the CTAC-seed solution. Afterward, 6 mL of 0.5 mM $HAuCl_4$ is injected to the mixture and vigorously stirred for 30 sec. The entire solution is left undisturbed at 28 ^oC for 15 min. The final products are isolated by centrifugation at 14,000 rpm for 30 min followed by careful removal of the supernatant. 1 mL of 20 mM CTAC is added to the pellet and the mixture is sonicated briefly to disperse the pellet.

80 nm sized Au nanosphere preparation*:* 2 mL of 0.1 M CTAC solution is mixed with 130 μL of 10 mM ascorbic acid. tion. 5 μL of 10 nm sized Au nanosphere solution is injected into the mixture. Afterward, 2 mL of 0.5 mM $HAuCl_4$ is followed by dropwise adding to the mixture using a syringe pump at an injection rate of 2 mL/hr. The final products are isolated by centrifugation at 14,000 rpm for 10 min followed by careful removal of the supernatant. 1 mL of 20 mM CTAC is added to the pellet and the mixture is sonicated briefly to disperse the pellet.

A.2.2 Synthesis of Janus-typed TiO_2 Capped Au Nanosphere

50 μL of Au nanosphere solution is diluted with 950 μL of DI-water. 500 μL of AuNS is followed by adding 500 μL of 0.25 wt. % of cellulose solution in IPA, and is undisturbed overnight. 250 μL of DI-water, 900 μL of IPA, 200 μL of NH_3 solution, and 50 μL of 1 mM TDAA solution are mixed with 1 mL of AuNS mixture and are followed by gently shaking for 18 hr using Eppendorf thermomixer. The final products are isolated by twice centrifugation at 9,000 rpm for 10 min followed by careful removal of the supernatant and resuspension with 1 mL of IPA. 1 mL of DI water is lastly added to the pellet and the mixture is sonicated briefly to disperse the pellet.

Appendix 3. Sequential Synthetic Steps of Multi-component Nanostructures

A.3.1 Synthesis of Au NR

High quality homogeneous Au NRs were prepared by a facile synthesis procedure.[23]

***Seed preparation**:* Seed preparation is identical with A 2.1.

***NR Growth**:* 3.6 g of CTAB and a certain quantity of NaOL were mixed in 196 mL of DI-water in a 500 mL Erlenmeyer flask. The solution was heated with occasional agitation until all the CTAB was dissolved. The mixture was allowed to cool down to 30 ^{o}C and 4 mM $AgNO_3$ as detailed in Table S3.1 was then added under stir at 700 rpm for 15 min. Afterward, 4 mL of 25 mM $HAuCl_4$ was added to the mixture and kept undisturbed at 28 ^{o}C for 90 min. The yellowish color of growth solution turned to colorless. HCl was added to the solution (Table A3.1) and the mixture was stirred at 400 rpm for 15 min. Finally, 500 μL of 0.064 M ascorbic acid was injected into the growth solution, and the mixture was vigorously stirred at 1200 rpm for 30 sec. A small amount of the seed solution according to the table S3.1 was then injected, and the solution was stirred for 30 sec before left undisturbed at 28 ^{o}C for 12 hr to complet0e the growth process. 40 mL of the final products were isolated by centrifugation at 8,000 rpm for 15 min followed by careful removal of the supernatant. 10 mL of DI-water was added to the pellet and the mixture was sonicated briefly to disperse the pellet. This Au NR stock solution was directly used for the growth of Au/TiO_2 nanodumbbell structure.

CTAB (g)	$AgNO_3$ (mL)	Seed (mL)	HCl (mL)	NaOL (g)	Average length (nm)	Average diameter (nm)	Figure number
3.6	5.0	0.16	0.84	0.4936	26	62	**Fig.3.3a**
3.6	7.2	0.16	0.84	0.4936	21	76	**Fig.3.3b**
3.6	9.6	0.08	0.6	0.4936	21	86	**Fig.3.3c**
3.6	9.6	0.08	1.2	0.4936	20	111	**Fig.3.3d**
3.6	4.8	0.08	0.84	0.6172	38	92	**Fig.4.3b**
3.6	3.6	0.08	0.84	0.6172	37	86	**Fig.4.3a**

Table A 3.1. Growth conditions for synthesized AuNRs.

A 3.2. Synthesis of Au/TiO_2 Nanodumbbell Structure

The Au/TiO_2 nanodumbbell structure was prepared by a slightly modified method by Wu et al.[24]

5 mL of fabricated Au NR stock solution was centrifuged at 5500 rpm for 8 min and the supernatant was carefully removed. The isolated product was dispersed into 5 mL of 0.2 M CTAB solution and 6.5 mL of DI-water. The purchased $TiCl_3$ solution and 20 mL of DI -water in a 125 mL Erlenmeyer flask were bubbled with N_2 for 10 min, respectively. 0.9 mL of $TiCl_3$ was then injected to 20 mL of DI-water under moderate stirring. Afterward, 2.2 mL of 1 M $NaHCO_3$ was added dropwise with the speed of 0.05 mL/s to the $TiCl_3$ solution and the color of the solution turned into dark purple. (Note: The same Au/TiO_2 nanodumbbell structure was obtained with different addition speed of bicarbonate within the range between 0.02 mL/s and 0.1 mL/s. The $TiCl_3$ from Fisher Scientific is a key parameter to optimize the condition of the synthesis.) Under moderate stirring, the Au NR stock solution was then added into the dark purple solution immediately. The mixture was kept stirring for 45 min followed by centrifugation at 5500 rpm for 8 min and washing with ethanol twice. The final isolated product was dispersed in 10 mL DI-water.

A 3.3. Photodeposition of Metal on Both Tips of Au/TiO_2 Nanodumbbell Structure

To determine the extinction at the wavelength of longitudinal localized surface plasmon resonance (LSPR), the stock solution of Au/TiO_2 was measured with a UV-Vis spectrometer with 1 nm resolution and 1 cm path length. The optical density of Au/TiO_2 solution was adjusted to OD 1 at the peak wavelength of longitudinal LSPR.

5 mL of Au/TiO_2 solution with the OD 1 was mixed with 4.5 mL of DI-water and 500 µL of 10 mM mPEG-SH solution. The mixture is shortly sonicated and is left undisturbed for 3 hr. The unreacted mPEG-SH was purified by centrifugation at 6000 rpm for 10 min. 10 mL of MeOH with different amount of metal precursor was mixed with the pellet of Au/TiO_2. Herein, for Pd, 50 µL of H_2PdCl_4 was used. For Pt, 20 µL of K_2PtCl_4 was used. For Ag, 20 µL of 20 mM $Ag(NO_3)_2$ was used. For Cu, 50 µL of 20 mM $Cu(NO_3)_2$ was used. The suspension was irradiated using 365 nm UV lamp for 15 min. The unreacted precursors were purified by centrifugation at 6000 rpm for 10 min. The cleaning process was repeated twice with MeOH, and the final pellet was redispersed in 5 mL of DI-water for the following process.

A 3.4. Photodeposition of Metal Oxide on the Side of Au/TiO_2 Nanodumbbell Structure

The stock solution of 1 M potassium borate buffer (pH 9.5) was prepared using 61.83 g of H_3BO_3 in 800 mL of DI-water. The stock solution of the buffer was titrated to pH 9.5 with 1 M KOH solution and finally adjusted to 1 L of total volume.

4.5 mL of Au/TiO_2 solution with the OD 1 was mixed with 500 µL of 1 M potassium borate buffer (pH 9.5) in an 8 mL glass vial (Fig A 3.1a). Afterwards, 250 µL of freshly prepared 2 M sodium persulfate solution and 31 µL of 10 mM $Co(NO_3)_2$ solution was added. Sodium persulfate was used as an electron scavenger. Prior to irradiation, the mixture was briefly sonicated for 1 min to fully disperse the nanoparticles. For photodeposition of CoO_x, broadband mounted light-emitting diode (MBB1L3, Thorlabs, 470-850 nm) was used as a light source to exclude the excitation of TiO_2. The mixture was illuminated with an intensity of 10 $mWcm^{-2}$ for 5 min from the bottom of the vial as shown in Fig. A3.1b. The intensity was calibrated at the air/glass interface placed a power meter on the bottom of the vial. Room light irradiation was cut off by aluminum foils. The unreacted precursors were purified by centrifugation at 5500 rpm for 8 min. The cleaning process was repeated twice, and the final pellet was redispersed in 5 mL of DI-water for the following process.

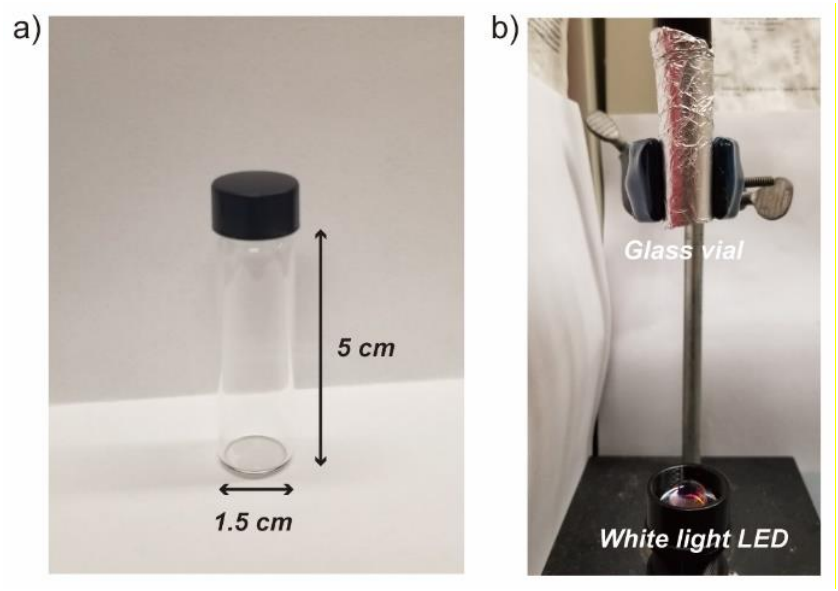

Figure A 3.1. a) Photograph of the used 8 mL scintillation vial (5 cm of height and 1.5 cm of diameter). b) Real image of the photodeposition setup.

A 3.5. Photodeposition of Pd on Both Tips of $Au/TiO_2/CoO_x$ Nanostructure (n=4)

The stock solution of H_2PdCl_4 was prepared by mixing 0.3546 g of $PdCl_2$ with 20 mL of 0.2 M HCl solution under moderate stir for 3 h to obtain a clear orange solution of H_2PdCl_4. To prepare 20 mM H_2PdCl_4 solution, the solution was diluted with 80 mL of DI-water. 2.5 mL of $Au/TiO_2/CoO_x$ stock solution with the OD 1 and 2.5 mL of methanol were mixed with 25 µL of 20 mM H_2PdCl_4 solution in an 8 mL glass scintillation vial. Methanol was used as a hole scavenger. The mixture was illuminated by the broadband mounted LED with the intensity of 10 $mWcm^{-2}$ for 12 min. The sample vial was covered by an aluminium foil to block the room irradiation. To remove unreacted Pd precursors, the solution was centrifuged at 5,500 rpm for 8 min and the isolated pellet was resuspended in 5 mL of MeOH for subsequent photodeposition of Cr_2O_3.

A 3.6. Photodeposition of Cr_2O_3 on Both Tips of $Au/TiO_2/CoO_x/Pd$ Nanostructure (n=5)

The Cr_2O_3 coated nanostructures were prepared using a modified method by Domen et al.[71] 10 µL of 20 mM K_2CrO_4 solution was added to the re-suspended $Au/TiO_2/CoO_x/Pd$ solution in 5 mL MeOH. The solution was then exposed to the broadband LED with the intensity of 10 $mWcm^{-2}$ for 8 min. The final product was cleaned by centrifugation one time with 5 mL of MeOH and twice with 5 mL DI-water, respectively.

Appendix 4. Optical and Structural Characterization

4.1 UV- vis Spectroscopy

The optical measurements were performed in DI-water. The absorption spectra were collected using a Shimadzu UV-3600 UV-VIS spectrophotometer with 1 nm resolution. The path length of the cuvette was 1 cm. Prior to the measurements, 1 mL of DI-water in the clean cuvette was used to obtain a blank baseline.

4.2 High-resolution TEM

To prepare the stock sample for TEM analysis, 50 μL aliquot of the nanoparticle solution was added to 1 mL of DI-water. The sample was centrifuged at 5,500 rpm for 8 min, the supernatant was carefully removed, and the isolated product was resuspended in 50 μL of DI-water. 5 μL of this solution was pipetted onto a standard carbon TEM grid (Electron microscopy Sciences, CF-400-Cu). The TEM grid with the sample was fully dried in a vacuum desiccator at room temperature before TEM imaging. TEM imaging was performed on a Tecnai G2 T20 S-TWIN TEM operating at 200 kV with a LaB_6 filament. All the images were taken using a Gatan Orius SC200 CCD camera.

4.3 HAADF-STEM-EDX Analysis

All the high resolution STEM-EDX hypermaps, as well as STEM-HAADF images, were acquired on an FEI TitanX 60-300 microscope using a Fischione high-angle annular dark-field (HAADF) detector with an inner semiangle, β, of 63 mrad. The EDX detector used was the FEI Super-X windowless detector with a solid angle of 0.7 steradians equipped with windowless silicon drift detectors. Samples for imaging were prepared on ultrathin carbon film transmission electron microscopy grids (Electron Microscopy Sciences CF400-Cu) by dropcasting a 5 μL of dispersed nanoparticles on the carbon-side and drying under vacuum for at least 24 hours prior to imaging. All elemental maps and HAADF images were collected at an accelerating voltage of 300kV and at a screen current of 375 pA over a 5-minute period with drift correction enabled at a pixel dwell time of 10 ms. Image acquisition Bruker Esprit 1.9 software was used for data acquisition, subsequent elemental analysis, and generation of line scans. In figures, undesignated signals from environmental impurities; Cu signal from the used TEM grid and Mo signal from the clip which was a part of the holder.

Appendix 5. Electrochemical Characterization

5.1 Electrode Preparation

The glassy carbon (GC) working electrode was polished with alumina polishing powder (0.05 μm, MicroPolish) prior to use. The working electrode was prepared via a drop-casting method. A 1 mL nanocrystal aqueous solution with an OD of 1 was centrifuged and concentrated to 50 μL by removing excess solvent. The nanocrystals were re-dispersed via sonication. A total of 10 μL of this concentrated solution was drop-casted onto the GC working electrode by depositing 2 μL of aliquot and allowing the solvent to evaporate. This drop-casting procedure results in an approximate loading of 0.5 μg mm^{-2} based on the extinction coefficient of gold nanorods.

5.2 Electrochemical Testing

A 1.0 M potassium borate buffer (pH 9.5) electrolyte prepared with H_3BO_3 and KOH was used for all electrochemical experiments. A digital potentiostat was used to collect the electrochemical data (SP-200, Bio-Logic Science Instruments). A 25 mL three-neck round bottom flask was used as the electrochemical cell (Chemglass Life Sciences), with a 3 mm diameter GC working electrode (CH Instruments), a mercury/mercury(I) sulfate reference electrode (MSE, CH Instruments), and a carbon rod counter electrode. The MSE standard potential is 0.64 V vs. the normal hydrogen electrode (NHE), and this was corrected to the reversible hydrogen electrode (RHE) at pH = 9.5 using the Nernstian pH dependence of the RHE. Cyclic voltammograms were collected at a scan rate of 40 mV s^{-1} under rigorous stirring. (Fig. 4.6)

Appendix 6. Photocatalytic Measurements

6.1 Photon Flux

The spectrally averaged photon energy (above 400 nm in the solar spectrum) was taken as 4.0×10^{-19} J.[39] The xenon lamp as a light source with a 400 nm long pass filter was carefully adjusted to the 1 sun illumination (AM 1.5G) with a calibrated Si photodiode (FDS1010-CAL, Thorlab), and the total illumination intensity was 100 $mWcm^{-2}$ (Fig. A 6.1) With these values, the mole of the incident photons per second was calculated to be 3.26 x 10^{-7} einstein s^{-1} cm^{-2}. The reactor was covered by an aluminum foil leaving small exposure space on the side wall for the illumination of the xenon lamp. We assumed that all the photons irradiated by the Xe lamp are absorbed by the sample, which is an overestimation of the number of photons absorbed due to scattering.

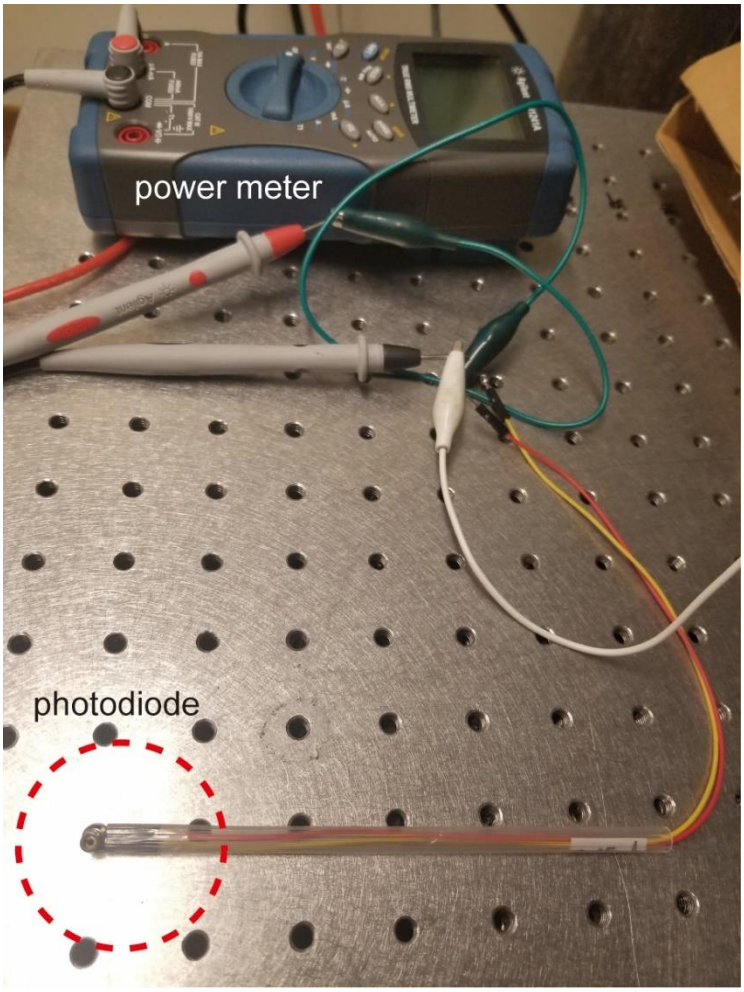

Figure A 6.1. The real image of customized built photodiode setup for 1 sun calibration.

6.2 Apparent Quantum Yield and Mass Efficiency

The apparent quantum yield (AQY) of integrated photocatalyst with a two-photon excitation process was defined by 2 × (4 × rate of O_2 generation) / (rate of photon absorption). With the G value being 6.6 ± 0.15 $nM \cdot s^{-1}$ and the volume of the sample solution being 1.5 mL, the rate of O_2 generation is calculated as $10.0 \pm 0.2 \times 10^{-12}$ $mol \cdot s^{-1}$. The aperture size of the reactor is 1 cm^{-2}, and the upper bound for the rate of photon absorption is 3.26×10^{-7} einstein s^{-1}. The apparent quantum yield defined as 2 × (4 × rate of O_2 generation) / (rate of photon absorption) was calculated as 0.024% for the integrated photocatalyst.

The mass efficiencies were calculated using the mass of the integrated photocatalyst and the rate of O_2 generation. To calculate the mass of the integrated photocatalyst, we referred to the theoretical extinction coefficient of the AuNR reported by Park et al.[S5] The extinction coefficient was extracted to 2.76×10^{10} $Lmol^{-1}cm^{-1}$ with the average dimension of our structure. With the unit cell's volume of Au which is 0.0679 nm^3 and molar mass of Au, the mass of one AuNR was calculated as 5.53×10^{-16} g. Since the optical density of the solution was set to 1 and the optical path length of the cuvette was 1 cm, the concentration of the particle in 1.5 mL was calculated as 3.62×10^{-11} M. With these values, the mass of AuNR was extracted to 18.1 μg. With the density of amorphous TiO_2 being 3.8 g/cm^3 and the measured volume of both caps being 8.3×10^4 nm^3, the mass of TiO_2 in 1.5 mL was calculated as 10.3 μg.[S6] The mass of other components was excluded due to negligible mass portion of the entire structure. The total mass of the integrated photocatalyst in 1.5 mL was 28.4 μg. The mass efficiencies were calculated as 0.36 $mmolg^{-1}h^{-1}$ for $Au/TiO_2/CoO_x/Pd$ nanostructure and as 1.27 $mmolg^{-1}h^{-1}$ for $Au/TiO_2/CoO_x/Pd/Cr_2O_3$ nanostructure.

6.3 The Excitation Spectrum of Xenon Lamp

The xenon lamp was used as an excitation source for the photocatalytic measurement. The excitation spectrum of xenon lamp was shown in Fig. A6.2. The xenon lamp with a 400 nm long pass filter was carefully adjusted to the 1 sun illumination (AM 1.5G) with a calibrated Si photodiode. All the *in situ* photocatalytic measurement were conducted by the calibrated the xenon lamp.

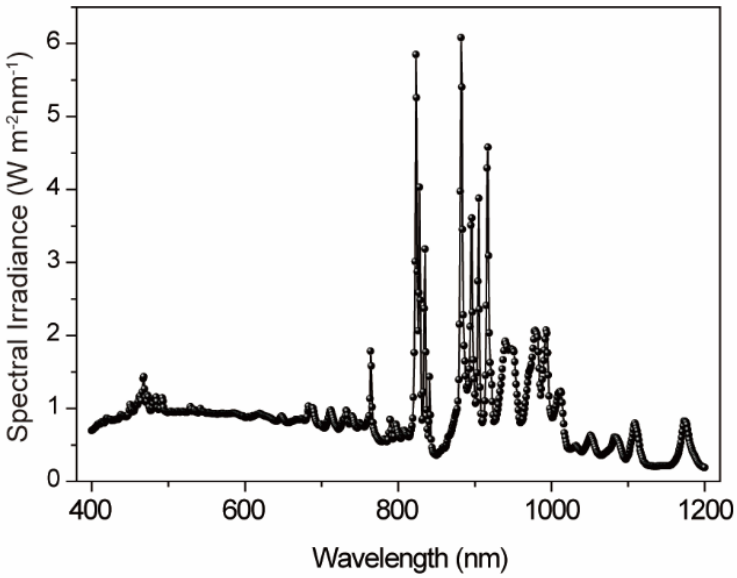

Figure A 6.2. The excitation spectrum of xenon lamp for photocatalytic measurement.

6.4 Calibration of Photocatalytic H_2 Measurement

The gas chromatography (GC) requires calibration curves of H_2 gas to analyze the exact amount of H_2 in the 1 mL loop. Here, the 1000 ppm H_2 gas with Ar and Ar gas (99.999% ultra high purity) are used to control the amount of injected H_2. The three-neck bottom flask is purged with the fixed amount of H_2 for at least 30 min prior to the injection to the GC. 10 mL of gas in the flask is injected to the GC to flush the 1 mL loop. The real GC data of H_2 gas in different concentration from 500 ppm to 20 ppm is shown in Fig. A 6.3a. Based on Fig. A 6.3a, each area of the peak is integrated above the fixed baseline. The calibration curve is shown in Figure A 6.3b.

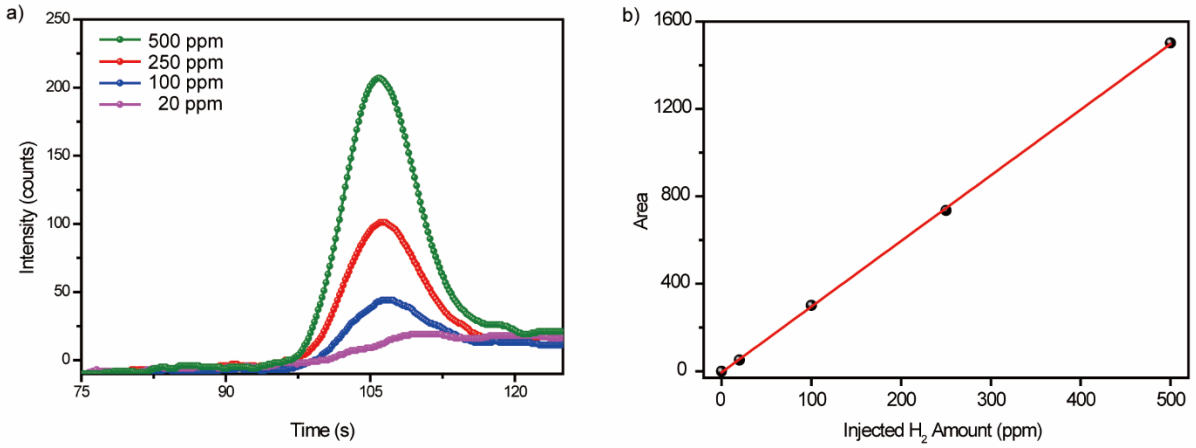

Figure A 6.3. a) Gas chromatograph spectra of H_2 gas with fixed concentrations. b) The area-based calibration curve of H_2 gas.

Appendix 7. Real images of photocatalytic O_2 and H_2 measurement setup

Here, the real images of experimental setup for both O_2 and H_2 photocatalytic setup are shown in Fig. A7.1 and Fig. A.7.2. The real dimension of the Clark electrode chamber is shown in Fig. A7.3.

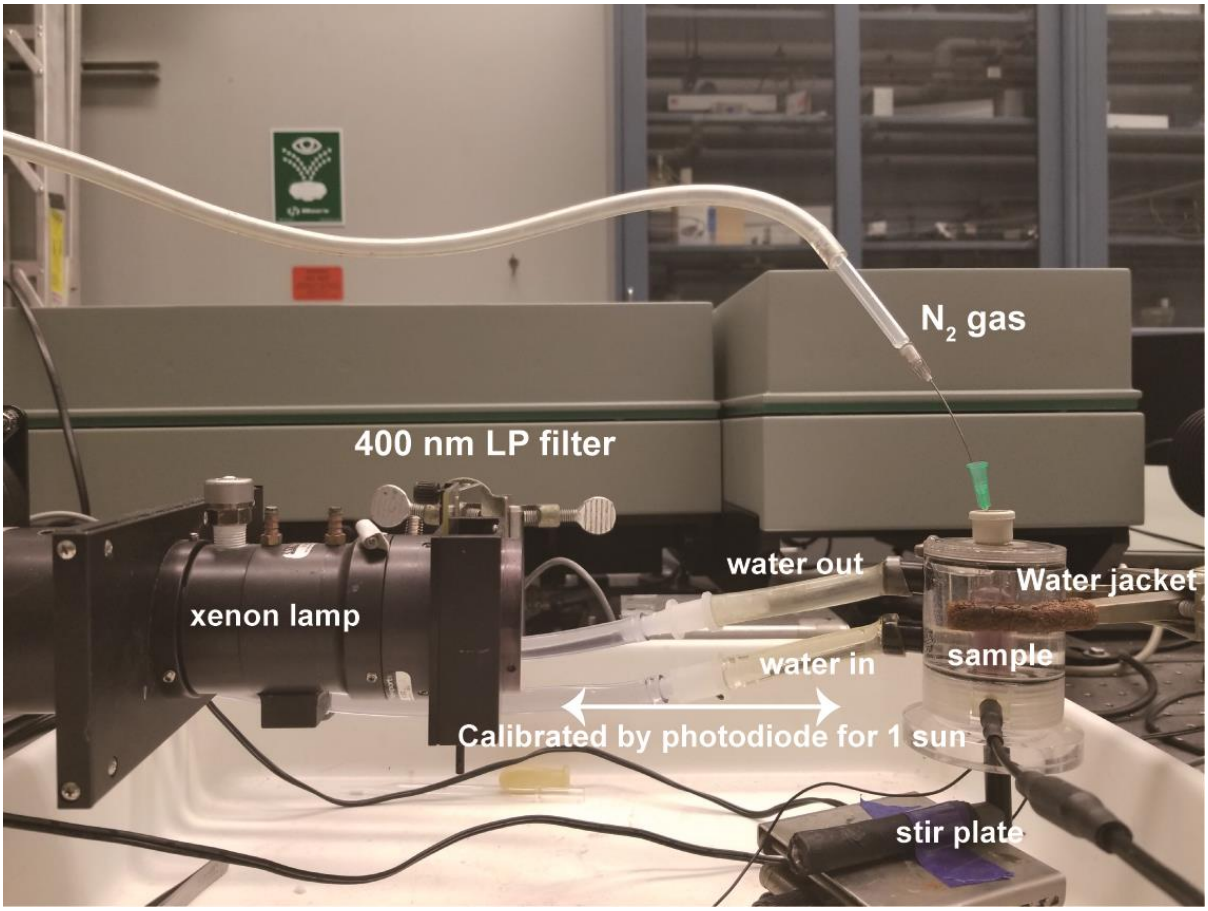

Fig. 7.1 Real image of photocatalytic O_2 evolution measurement setup

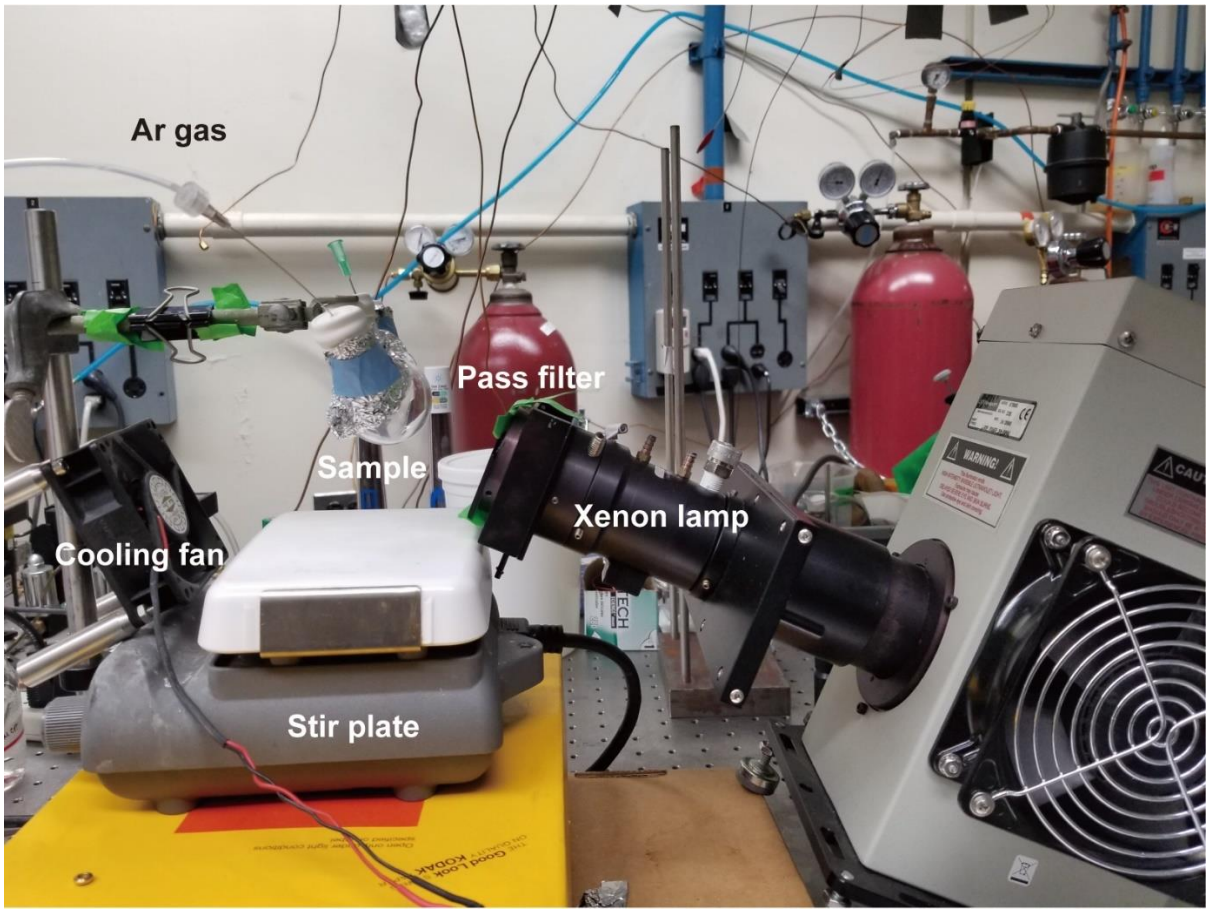

Fig. 7.2 Real image of photocatalytic H_2 evolution measurement setup

Fig. 7.3 Real image of the Clark electrode chamber. The diameter is 1 cm, and the height is 4.5 cm. Total capacity of this chamber is 2.5 mL.